RSC Advances

PAPER

Check for updates

Cephalexin-loaded polyvinyl alcohol/graphene oxide thin films as antibacterial wound dressing

Soroush Barkhordari, [ID] *[a] Soroush Yousefi, [ID] [b] Safa Momeni Badeleh, [ID] [c] Hossein Abdollahi, [ID] [d] Morteza Abazari [ID] *[e] and Abdolhmid Alizadeh [ID] [f]

In the present study, biodegradable polyvinyl alcohol/graphene oxide-based thin films were prepared as a topical drug delivery system *via* the solvent casting method for the loading and controlled release of the antibacterial drug cephalexin. Results showed that all the fabricated thin films had highly uniform and smooth-surface textures. The chemical structure and crystallinity of the samples were investigated by FTIR spectroscopy and XRD analysis, and the SEM and EDX techniques revealed the successful loading and uniform dispersion of cephalexin within the prepared films. Investigations on the thermal properties of the samples indicated that the thermal stability of the samples increased with the addition of graphene oxide, while it decreased with the addition of cephalexin. Water contact angle measurements revealed an increase in the hydrophobicity of thin films upon the addition of graphene oxide and cephalexin, and the final scaffolds displayed a contact angle of 104.6° ± 1.72°. The fabricated thin films also displayed pH-dependent degradation, swelling, and release behaviors in PBS solutions of pH 7.4 and 5.5. Moreover, a two-stage release profile was observed for drug-containing films during the liberation of cephalexin into release media. Additionally, the drug-containing films exhibited potent antibacterial activity against both Gram-positive and Gram-negative bacteria. Evaluating the cytocompatibility of the samples revealed desired cell viability up to 64 mg mL^{-1} during 24 h, and the toxic effect of the samples was increased in a concentration-dependent manner.

Introduction

Today, the development of various drug-delivery systems (DDSs) with diverse forms, shapes, and compositions for the effective and safe delivery of different pharmaceutical active agents (APIs) has garnered significant interest in both the scientific and clinical sectors. In fact, the conventional and traditional administration routes of many drugs and other active substances lead to insufficient therapeutic efficiency at the targeted sites and the possibility for the occurrence of various side and adverse effects.[1,2] As a result, several DDSs have been developed to cope with these problems and overcome their multivariate clinical and therapeutic impediments by implementing various site-specific and controlled delivery mechanisms.[3,4] Moreover, these systems provide effective and therapeutic concentrations of various APIs at the intended site of action and therefore diminish the need for their repeated administration, which is the leading cause of drug tolerance or drug insensitivity in the clinic.[5,6] In this context, various well-established DDSs maximize the value, application, and activity of numerous APIs and mitigate the unwanted and adverse effects caused by uncontrolled and excessive dosage and drug administration.[7-9]

Antibiotics represent the first-line medications used for treating various systemic and topical infections.[10,11] Amino-glycosides, cephalosporins, penicillins, sulfonamides, glyco-peptides, and fluoroquinolones are among the groups of antibiotic medications that are frequently prescribed.[12] Due to their broad-spectrum activity, antibiotics are extensively used for treating various infectious diseases, including secondary infected dermatitis, infected wounds, mild to moderate acne vulgaris, rosacea, and impetigo.[13] In most of these applications, the topical administration of antibiotics is preferred over systemic administration due to the diverse side and adverse effects of these substances in the oral route; furthermore, systemic administration causes the spreading of antibiotics throughout the body, resulting in low effective concentration of antibiotics at the infected site.[14,15] Alternatively, the topical

[a]Department of Organic Chemistry, Faculty Chemistry, Alzahra University, Tehran, 19938-93973, Iran. E-mail: br_soroush@yahoo.com; Tel: +989121300969

[b]School of Pharmacy, Zanjan University of Medical Sciences, Zanjan, Iran. E-mail: soroushyousefi834@gmail.com

[c]Department of Food and Drug Control, School of Pharmacy, Zanjan University of Medical Sciences, Zanjan, Iran. E-mail: safamo0568@gmail.com

[d]Department of Polymer Engineering, Faculty of Engineering, Urmia University, Urmia, Iran. E-mail: h.abdollahi@urmia.ac.ir

[e]Experimental and Applied Pharmaceutical Sciences Research Center, Urmia University of Medical Sciences, Urmia, Iran. E-mail: m.abazari119@gmail.com

[f]Department of Organic Chemistry, Faculty Chemistry, Alzahra University, Tehran, Iran. E-mail: ahalizadeh2@hotmail.com

delivery of antibiotics provides localized and targeted delivery options to the site of concern with an effective concentration, reduced toxicity, low cost, and feasible administration.[14,16] However, some issues are also conceivable for the topical delivery of antibiotics, such as the emergence of multidrug- and antibiotic-resistant bacteria, inherent limitations in treating superficial infections, and the possibility of inducing contact dermatitis. Therefore, developing state-of-the-art DDSs for the effective topical delivery of antibiotics to superficial infections and infected wounds is essential for achieving better treatment outcomes and minimizing undesired adverse events or toxicity.[17,18]

To date, a wide variety of DDSs with different shapes and compositions have been developed and considered for the topical delivery of antibiotics.[3,19–21] As a few examples, hydrogels, nanofibers, sheets, thin films, sponges, *etc.*, could be introduced. These platforms have been extensively utilized to incorporate antibiotic substances and release them into the infected area in a controlled and sustained manner.[22–24] Each platform presents its own advantages and disadvantages, based on its physicochemical and functional properties, as well as the anatomical and physiological conditions of the infected site.[25,26] Of these platforms, thin film-based scaffolds possess several benefits regarding topical drug delivery applications, such as facile production methods, uniform drug distribution and dose, increased bioavailability, lower incidence of irritation, and continuous drug release, in addition to providing a moist environment that favors most wound-healing processes.[27,28] Thin-film-based scaffolds can be produced *via* various fabrication methods, including spin coating, solvent casting, and drip coating, and are capable of incorporating and delivering a wide range of antibiotic materials, as well as other drugs.[29,30] In the fabrication of thin films, polymeric materials with good film-forming properties from synthetic and natural origins, such as polyvinyl alcohol (PVA), polyvinyl pyrrolidone (PVP), chitosan, sodium alginate, and cellulose derivatives, could be employed either individually or in composite forms.[31,32]

Among various polymeric materials, PVA showcases several advantages and superior characteristics regarding thin-film fabrications and applications.[33,34] PVA is a synthetic polymer with the general formula $[CH_2CH(OH)]_n$ that exhibits excellent film-forming ability, high hydrophilicity, and good physical and chemical stability, in addition to being inexpensive and commercially available. Owing to its vast beneficial physicochemical and functional properties, it is applied and considered in many technological and industrial applications, such as papermaking, textile warp sizing, as a thickener and emulsion stabilizer in polyvinyl acetate (PVAc) adhesive formulations, in a variety of coatings, electrospinning, and 3D printing.[35,36] However, the resultant PVA scaffolds and thin films exhibit poor mechanical properties and low stability in aqueous solutions due to their high affinity for water, which causes swelling of the products and can lead to failure under particular conditions and circumstances. Therefore, pre- or post-processing modification of PVA-based products is essential for enhancing their functional characteristics in specific applications.[36,37]

The combination of PVA with other polymeric and non-polymeric materials in the form of various composites offers a practical approach to modifying PVA scaffolds that can enhance their functional and product-oriented characteristics. As a result, numerous PVA-based composites have been developed in previous studies for various applications in different fields and areas.[38–40] In this regard, graphene oxide (GO) materials, as two-dimensional (2D) carbon-based nanomaterials, offer many beneficial features for modifying various polymer-based composites and scaffolds.[41,42] GO-based materials are generally produced through chemical oxidation of natural graphite or carbon nanofibers and play an important role in the design and development of various DDSs because of their desirable biocompatibility properties and facile functionalization with biomolecules and other pharmaceutical ingredients.[43] Moreover, GO materials exhibit remarkable mechanical, electrical, thermal, and barrier properties, as well as good hydrophilicity and a large specific surface area, which make them ideal for developing various medical and non-medical products in different fields and applications. Additionally, GO can be easily incorporated into many multilayer polymeric composites, such as PVA thin films for drug delivery purposes, to enhance their drug-loading capacities and promote the controlled or sustained delivery of various pharmaceutical and active agents.[44–47]

Although numerous studies have examined PVA/GO scaffolds and their properties[48–50] their use as drug-delivery systems for topical application and wound healing has not yet been explored. As a result, the present study is designed to fabricate PVA/GO-based thin films as a new and effective platform on which to load and topically deliver cephalexin (CPX), as a representative antibiotic, for the management and treatment of superficial infections and infected wounds. The intended scaffolds were prepared using the solvent casting method and thoroughly investigated for their physicochemical and functional characteristics as an antimicrobial wound dressing for wound healing applications.

Materials and methods

PVA (Mw = 145 000 and fully hydrolyzed), sodium nitrate (NaNO$_3$), sodium hydroxide (NaOH), and graphite powder ($\leq$20 μm) were obtained from Merck Chemical Company, Germany. CPX monohydrate was purchased from Danna Pharma Co. (Tabriz, Iran). Sulfuric acid (H$_2$SO$_4$), hydrogen peroxide (H$_2$O$_2$), potassium permanganate (KMnO$_4$), sodium nitrate (NaNO$_3$), hydrochloric acid (HCl), phosphate-buffered saline (PBS), and glycerol were acquired from Sigma-Aldrich, Germany.

Preparation of GO

GO was prepared by oxidizing natural graphite powder using the modified Hummers' method.[51] Briefly, 1 g of graphite powder was transferred into a 250 mL flask, which was placed in an ice bath containing 50 mL of concentrated H$_2$SO$_4$ and stirred cautiously. Then, 0.5 g of NaNO$_3$ was added to the flask and stirred with a magnetic stirrer for 24 hours. After this time, 6 g

of KMnO$_4$ was slowly added to the solution, and the reaction temperature was maintained below 20 °C. Next, the ice bath was removed, and the reaction mixture was stirred for 48 hours at 30 °C. In the next step, 100 mL of deionized water and 30 mL of H$_2$O$_2$ were added to the reaction mixture, and the resulting yellowish-brown solution was centrifuged at 4000 rpm for 6 min. The resulting precipitate was washed with a 10 : 1 (v/v) HCl solution and deionized water to purify the material. To this end, centrifuge tubes containing the suspension were filled with HCl solution and sonicated in an ultrasonic bath for approximately 5 min, followed by centrifugation at 4000 rpm for 6 min. Then, the supernatant was discarded, and this procedure was repeated four times using HCl and deionized water. The supernatant was then decanted off, and the precipitates (GO) were dried under vacuum at 50 °C.

Preparation of PVA thin films

To prepare PVA thin films, 5 g of PVA granules was dissolved in 100 mL of double-distilled water under stirring at 85 °C for 12 h. When the PVA was completely dissolved, 15% w/w glycerol was added as a plasticizer (based on the dry content of PVA), and the mixture was heated under reflux at 90 °C for 5 hours. The resulting clear PVA solution was cast on a glass mold and dried at ambient temperature.

Preparation of PVA/GO thin films

Similar to the preparation of PVA films, 5 g of PVA was dissolved in 100 mL of double-distilled water under stirring at 85 °C for 12 h. Then, 0.1 g of the prepared GO was added to the PVA solution, and the resultant solution was placed in an ultrasonic bath for 30 minutes to achieve uniform dispersion of the GO. Subsequently, 15% w/w glycerol was added, and the mixture was heated under reflux at 90 °C for 5 hours. Finally, the prepared solution was cast on a glass mold and dried at ambient temperature.

Preparation of CPX-containing PVA/GO thin films

The PVA/GO solutions were prepared as described in the previous section, and then 0.1, 0.2, and 0.3 g of CPX were added to the resultant solutions to prepare 2%, 4%, and 6% w/w CPX-containing solutions. The resultant solutions were stirred until the CPX was dissolved entirely, and then 15% by weight of glycerol was added. The obtained solutions were refluxed at 90 °C for 5 hours, cast on a glass mold, and then dried at ambient temperature.

Characterization

Film thickness

The thickness of thin films was determined using a digital micrometer (measuring range: 0–25 mm, resolution: 0.001 mm, accuracy: ±0.004 mm) by measuring at ten random locations on each film.

FTIR and ATR-FTIR analyses

A Thermo Nicolet, Avatar 370 spectrophotometer (Thermo Scientific, Madison, WI, USA) was used to investigate the structural properties and specific absorption peaks of the samples. The measurements were performed using the potassium bromide (KBr) disc technique with a resolution of 4 cm^{-1}. The attenuated total reflectance Fourier-transform infrared (ATR-FTIR) and FT-IR spectra of samples were recorded at 500–4000 cm^{-1} with a resolution of 4 cm^{-1}.

Morphological analysis

The morphological characteristics of the prepared thin films were examined using field-emission scanning electron microscopy (FESEM; Zeiss Sigma VP300, Germany) at an accelerating voltage of 5.00 kV. The samples were sputter-coated with gold (Nano-Structured Coatings Co. DSR1, Tehran, Iran), and images were acquired using SEM. Energy-dispersive X-ray (EDX) spectroscopy was used to investigate the elemental features and distribution of the fabricated samples.

XRD analysis

The crystal structures of the samples were analyzed with an X-ray diffractometer (XRD, PW1730, Philips, Netherlands). The scan was performed using Cu-Kα radiation ($\lambda = 1.54056$ Å) with a 2θ range of 5–80° and a scanning speed of 1°/min.

Thermal properties

The thermal properties and transitions of the samples were investigated by differential scanning calorimetry (DSC), thermogravimetric analysis (TGA), derivative thermogravimetry (DTG), and differential thermal analysis (DTA) using a DSC Q600 (DSC-TGA, TA Instruments, USA). The experiments were carried out in a nitrogen atmosphere using about 10 mg of samples sealed in aluminum pans. The samples were heated from room temperature to 650 °C. The heating rate was 10 °C min^{-1} in all cases. The variation of the crystallinity of thin films was estimated by the following equation:[52]

$$X_c = \frac{\Delta H_{PVA}}{\Delta H_{100}} \times 100 \qquad (1)$$

where ΔH_{PVA} is the enthalpy absorbed by the PVA-based thin films during the heating process, and ΔH_{100} is the enthalpy absorbed by the 100% crystalline PVA (138.6 J g^{-1}).[53]

Contact angle measurements

The hydrophilicity of the prepared thin films was investigated *via* a contact angle system (model CAG-20, Jikan, Iran). A drop of water was deposited on the scaffold surface, and the drop shape was analyzed by the JikanAssistant 3.5 software.

Degradation and swelling properties

The aqueous stability and swelling behavior of the films were investigated by gravimetric analysis. For aqueous degradation analyses, circular-shaped samples of the films with predetermined weights (M_i) were immersed in 15 mL phosphate-

buffered saline (PBS, pH 7.4 and 5.5) and incubated at 37 °C. Then, the samples were removed from the PBS media, dried at ambient temperature, and weighed again (M_f). The degradation percentage of the samples was calculated using the following equation.

$$\text{Degradation (\%)} = M_f/M_i \times 100$$

To determine the swelling ratio of the films, circular-shaped samples with known initial weights (M_w) were soaked in PBS at pH 7.4 and 5.5, and incubated at 37 °C. After specific time intervals (30 min), the samples were withdrawn, weighed again (M_d), and returned to the PBS media for the next time interval. The swelling ratio of the samples was calculated using the following formula.

$$\text{Swelling percentage (\%)} = [(M_w - M_d)/M_d] \times 100$$

Drug release studies

To investigate the release profiles of CPX from thin films, initially, the calibration curves of CPX in PBS at pH 7.4 and 5.5 and 275 nm (λ_{max} of CPX) were established. To this end, CPX solutions with concentrations of 10, 20, 50, 100, 150, and 200 ppm were prepared, and their UV-Vis absorbances were recorded using a PerkinElmer Lambda 35 UV/Vis spectrometer. The calibration curve of CPX was established using the absorbance of each solution against concentration. For drug release analyses, circular-shaped samples with known initial weights were soaked in 25 mL PBS at pH 7.4 and 5.5 and incubated at 37 °C in a shaking incubator. At predetermined times, 1 mL of the release solution was removed for UV/vis analysis and replaced with 1 mL of fresh medium. The cumulative amount of CPX liberated in the studied time range (0–480 min) was then evaluated.

The *in vitro* CPX release profiles of the samples were further elaborated using the zero-order, first-order, Higuchi, and Korsmeyer–Peppas kinetic release models:[54–56]

$$Q_t = Q_0 + k_0 t \tag{2}$$

$$Q_t = Q_0 e^{-k_1 t} \tag{3}$$

$$Q_t = k_h t^{1/2} \tag{4}$$

$$Q_t = k_m t^n \tag{5}$$

Antibacterial activity

The antibacterial activity of the films was investigated by the disk diffusion and viable cell count tests against Gram-positive (*Staphylococcus aureus*, *S. aureus*, Gr$^+$, ATCC 25923, facultative anaerobe) and Gram-negative (*Escherichia coli*, *E. coli*, Gr$^-$, ATCC 25922, facultative anaerobe) bacteria. Both bacterial strains were supplied by the Microbiology and Biotechnology

Lab (University of Tehran, Iran). In the disk diffusion test, a 0.5 McFarland standard suspension (1.5×10^8 CFU mL^{-1}) was prepared from freshly cultured bacteria. Then, the agar surface was inoculated using a swab dipped in the bacterial suspension. The prepared films were punched into circular pieces (0.5 cm in diameter), placed on the bacterial-inoculated agar surface, and incubated at 37 °C for 24 h. The inhibition zone diameters were measured to the nearest millimeter using ImageJ 1.52v software (National Institutes of Health, USA, http://imagej.nih.gov/ij/).[57–59]

In the viable cell count method, a 0.5 McFarland standard suspension was prepared that was identical to that used for the disk diffusion test. After dilution with physiological serum, the prepared samples were contacted with a specific volume (1 mL > V > 0.4 mL based on the sample volume and area) of the bacterial suspension for 1, 3, and 6 h. Next, about 0.1 mL aliquots of the resulting suspensions were spread out on the previously prepared agar plates and incubated at 30 ± 2 °C. After 24 h, the number of bacterial colonies was counted with the colony counter. The number of colonies per volume (CFU mL^{-1}) was calculated using the following formula.[60,61]

$$\text{CFU/mL} = (\text{no. of colonies} \times \text{dilution factor})/\text{volume of the culture plate}$$

The percentage and logarithmic reduction were calculated based on the CFU/mL results.

MTT cell viability assays

The cytotoxicity of the films was assessed with the MTT assay according to our previous studies.[22,62,63] DMEM high glucose was used as a medium for culturing the normal cells (human dermal HFF-1 cell line, obtained from the Animal Biology Department, University of Tehran, Iran). The HFF-1 cells were grown in a humidified incubator at 37 °C and 5% CO$_2$. After reaching the desired confluency (80%), the cells were harvested and counted. Then, the resultant cells were seeded in 96-well plates (1×10^4 cells per well) and incubated for 24 h at 37 °C and 5% CO$_2$. The prepared scaffolds were immersed in PBS solutions for 24 h and then homogenized with a high-shear homogenizer to obtain homogeneous solutions. After 24 h of cell seeding, different concentrations of the prepared solutions were added to each well and incubated for another 24 h. Subsequently, 20 μL of the MTT solution (5 mg in 2 mL PBS, pH 7.4) was added to each of the 96-well plates and incubated at 37 °C for 4 h until the formazan product was developed (purple color). Next, the solution in each well containing media, unbound MTT, and dead cells was removed by the suction method, and 100 μL of DMSO was added to each well. The optical densities (OD) of the cells were measured with a microplate reader at 570 nm. Prior to the measurements, the cells were shaken. All analyses were done in triplicate, and the cell viability/increase was presented in percentages in reference to control cells (untreated cells).

Statistical analysis

All analyses in this study were conducted in triplicate, and the results are represented as mean ± standard deviation. The significant differences between groups were determined by the *t*-test or one-way analysis of ANOVA. The results were considered statistically significant when the *P* value was equal to: $*p < 0.05$, $**p < 0.01$, and $***p < 0.001$. The data analysis software was SPSS v26 (IBM SPSS Statistics, Chicago, IL, USA).

Results and discussion

In the present study, PVA/GO-based thin films were fabricated using the solvent casting method and loaded with CPX in order to prepare antimicrobial scaffolds for topical drug delivery and the treatment of superficial infections and infected wounds. To this end, GO was synthesized *via* the chemical oxidation of natural graphite and accompanied by PVA to form a polymeric scaffold for effective loading and delivery of CPX in treating infected wounds. The preparation method of the scaffolds is shown schematically in Fig. 1A–C. In the following sections, the physicochemical and functional properties of the resultant scaffolds will be discussed.

The images and thicknesses of the fabricated thin films, with or without CPX, are depicted in Fig. 1D. As we can see, the pure PVA solution yielded a highly transparent film. However, the GO- and CPX-containing films produced black films primarily due to the presence of black-colored GO in these films. The thickness of the prepared thin films ranged from 0.053 to 0.096 mm across different samples and increased with the addition of GO and CPX to the formulations. It is worth noting that all the prepared solutions in this study resulted in the formation of highly uniform, physically stable, and smooth-surfaced thin films, as evident from Fig. 1D.

The FTIR spectra of the starting materials (GO and CPX), as well as the fabricated PVA, PVA/GO, and PVA/GO/CPX, are depicted in Fig. 2A. The FTIR spectrum of the synthesized GO showed several distinct peaks at the $400–4000$ cm^{-1} wavenumber range. For better visualization of the GO FTIR peak intensity, a separate spectrum is also provided for GO in Fig. 2A. In these figures, the broad peak at 3446 cm^{-1} in the GO spectrum is attributed to the stretching vibration of the hydroxy groups. As we can see, this peak is broader in the FTIR spectra of all the other samples, indicating their higher hydrophilicity (especially PVA), which enables them to adsorb significant amounts of water. The twin peaks observed at 2854 and 2925 cm^{-1} were attributed to the symmetrical and asymmetrical vibration of the methyl and methylene groups, respectively.[22,24,64] The presence of these functional groups in the GO structure refers to the Kirigami model of GO proposed previously.[65] These peaks were also observed in the FTIR spectra of pure CPX and PVA film (specified by a single asterisk), which indicates the presence of methylene groups in the chemical structure of CPX and the polymeric backbone of PVA. However, the 2854 and 2925 cm^{-1} peaks did not appear in the FTIR
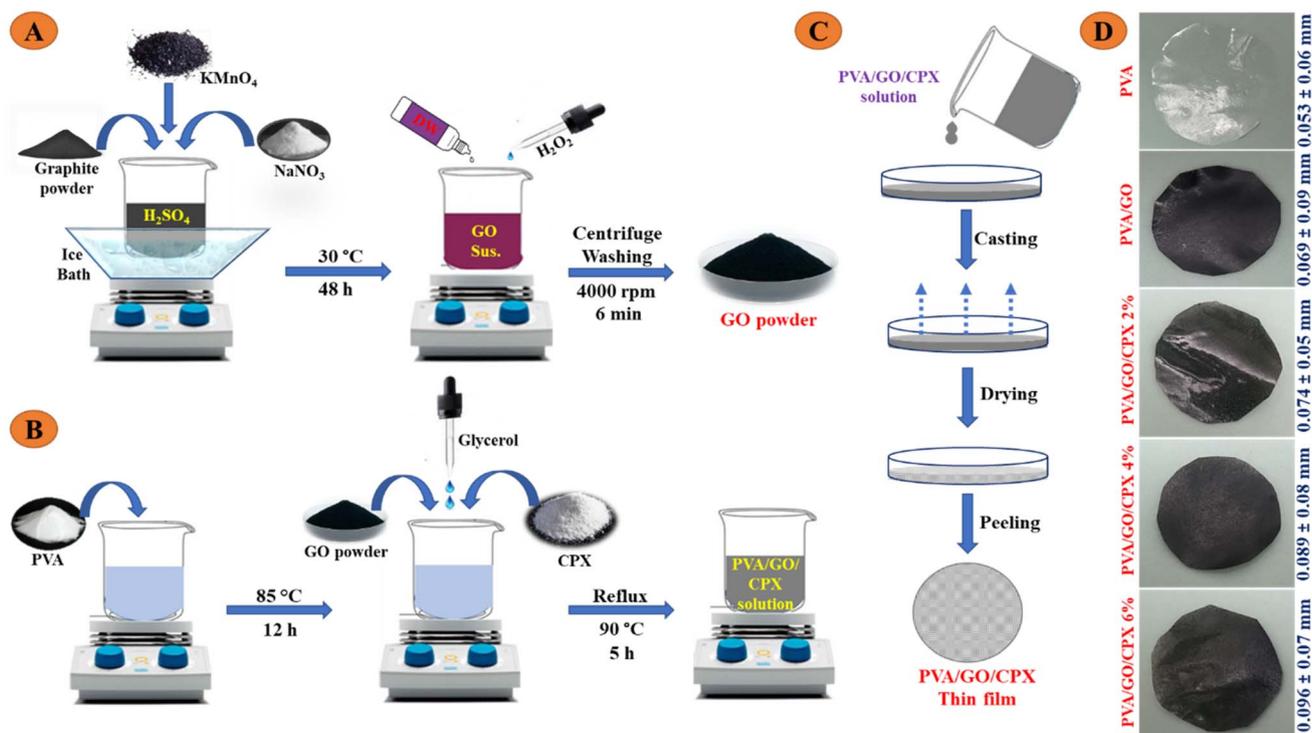

Fig. 1 Schematic of the CPX-loaded PVA/GO-based thin films. (A) Preparation of GO by the chemical oxidation of natural graphite powder. (B) Preparation of the PVA/GO/CPX casting solution. (C) Fabrication of the CPX-loaded PVA/GO thin films with different CPX content (2%, 4%, and 6%w/w) using the solvent-casting method. (D) Images and thicknesses of the prepared films with different compositions and various amounts of drug. (DW: Deionized water).
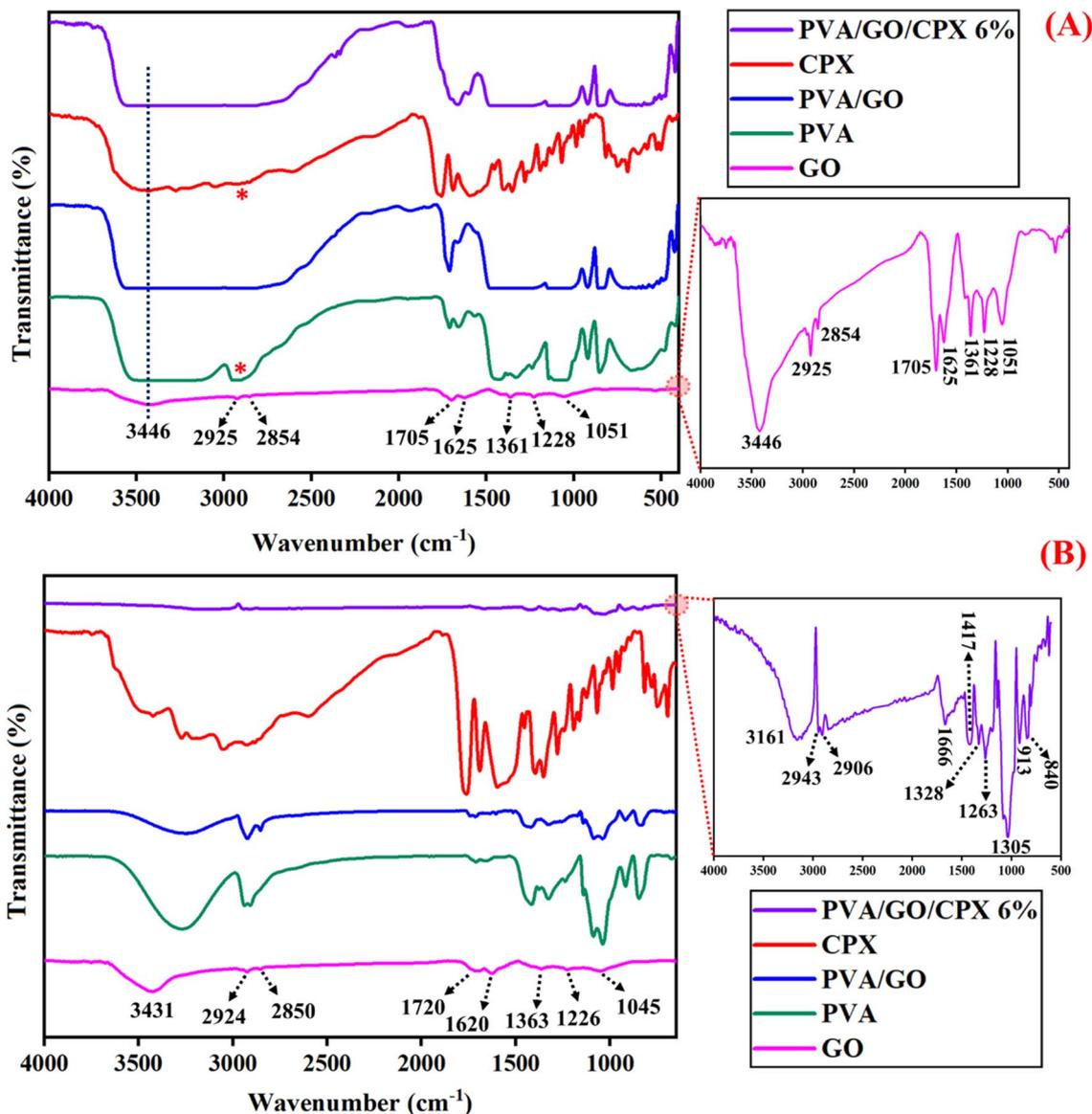
Fig. 2 (A) FTIR and (B) ATR-FTIR spectra of the GO, CPX, and fabricated thin films, representing their chemical structure and presence of different functional groups.

spectra of the PVA/GO and PVA/GO/SPX, which were probably covered by the broad peak of the hydroxyl groups in this region. The next peak at 1705 cm^{-1} in the FTIR spectra of all samples corresponds to the carboxyl groups of GO, CPX, and PVA samples. The latter is because of the remaining acetate groups in the PVA structure. The peak at 1625 cm^{-1} is attributed to the C=C groups and was observed in the FTIR spectra of all the samples. The three peaks with medium intensity at 1051, 1228, and 1361 cm^{-1} are related to the presence of C–O–C, C–O, and C–OH functional groups of the samples, respectively. These peaks are absent in the FTIR spectra of composite thin film samples (PVA/GO and PVA/GO/CPX), which could be explained by the possible interactions between their individual constituents during the thin-film preparation process. The spectra obtained in this study for the investigated samples showed good agreement with the results reported in previous studies.[22,64,66]

Similar peaks to those in the FTIR spectra were also observed in the ATR-FTIR spectra, with a slight displacement observed in the wavenumber of the respective peaks (Fig. 2B). In this regard, the peaks at 3431, 2924, 2850, 1720, 1620, 1363, 1226, and 1045 cm^{-1} were observed in the ATR-FTIR spectra of the samples, in accordance with the functional groups assigned in the FTIR spectra. However, in comparison to the FTIR spectra, the peak's intensities were significantly decreased, especially for the PVA/GO/CPX 6% sample. This could be attributed to the limited depth of penetration of the infrared light in ATR-FTR compared to that of the FTIR technique.

The XRD analysis of the GO, CPX, and fabricated thin films was conducted to assess their crystallinity and uniform dispersion within the thin-film matrices. From the results presented in Fig. 3, the as-synthesized GO showed two distinctive diffraction peaks at 12.4° and 42.76°, corresponding to its (001)
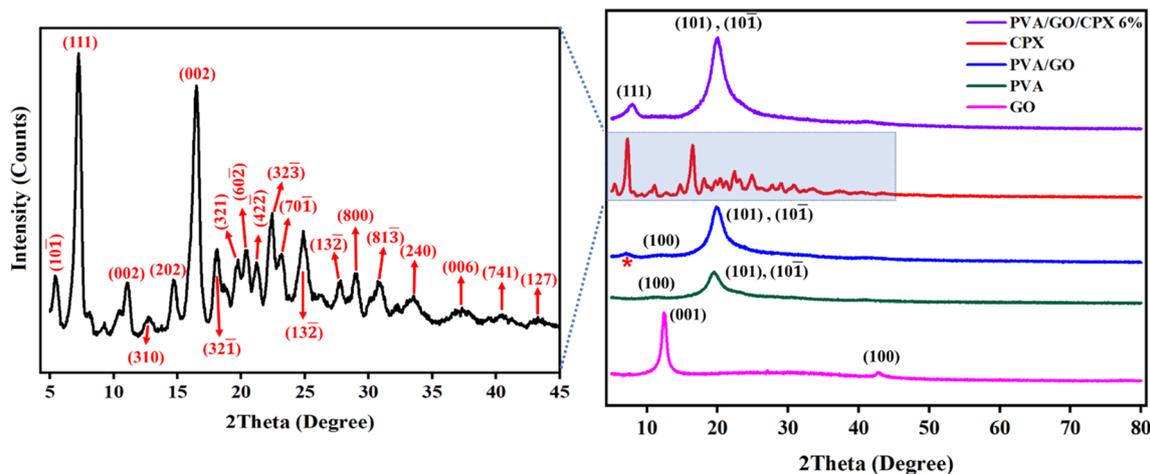
Fig. 3 XRD patterns of the GO, CPX, and fabricated thin films.

and (100) crystalline planes, respectively. Similarly, the pure PVA thin film exhibited two characteristic peaks at 11.52° and 19.52°. The peak at 11.52° related to the (100) diffraction plane of PVA, while the 19.52° peak was attributed to its (101) and (10$\bar{1}$) diffractions. These findings are in good agreement with the reports on GO and PVA materials in previous studies.[22,67,68] The PVA/GO thin films exhibited the characteristic peaks of the PVA at 11.52° and 19.52°, corresponding to the (100), (101), and (10$\bar{1}$) diffractions. However, the incorporation of GO into the PVA matrix resulted in the complete disappearance of the GO peaks. It is worth noting that the diffraction peak of the PVA sample at 19.52° was significantly amplified in the PVA/GO composite film pattern. Similar results were also reported in previous studies in which the intensity of the PVA peak at 19.52° increased with the addition of GO in a concentration-dependent manner.[67,68] Moreover, an additional peak at 7.08° (indicated with a red asterisk) appeared in the XRD diffractogram of the PVA/GO sample, which is absent in the XRD pattern of individual PVA and GO samples. These results indicate good incorporation, desired exfoliation of entire GO nanosheets, and uniform dispersion of GO in the PVA matrix that led to the formation of new crystalline domains and improved crystallinity of the resultant PVA/GO thin films. As a result, following the addition of GO into the PVA matrices, the semi-crystalline fingerprints of PVA were modified, and an enlarged, sharp peak (increased width and sharpness) was observed together with an additional peak, which suggests the improved crystallinity of the nanocomposites. The XRD pattern of the CPX (Fig. 3) exhibited several diffraction peaks at 5–45° corresponding to its crystalline structure. For better visualization, the diffractogram of CPX is also expanded in Fig. 3. The peak assignment of the CPX sample was performed according to the peak values of 2θ and Miller indices (hkl) and was confirmed using the International Centre for Diffraction Data (ICCD) crystallography databases (Reference number: 00-040-1653). Accordingly, the following main XRD peaks at the specific 2θ values with related Miller indices were identified for the pristine CPX sample, which is also assigned and specified to each peak

of the CPX diffractogram shown in Fig. 3 (values in degrees): 5.43 (10$\bar{1}$), 7.24 (101), 11.05 (002), 12.64 (310), 14.72 (202), 18.10 (32$\bar{1}$), 19.71 (321), 20.39 (60$\bar{2}$), 21.2 (42$\bar{2}$), 22.41 (32$\bar{3}$), 23.14 (70$\bar{1}$), 24.88 (13$\bar{2}$), 27.75 (800), 28.99 (81$\bar{3}$), 30.87 (240), 33.46 (006), 40.44 (741), and 43.37 (127). Based on the results, the pristine CPX showed a highly crystalline structure, which corresponded to a monoclinic crystal system with the unit cell parameters of $a = 27.0670$ Å, $b = 11.9190$ Å, $c = 16.7880$ Å, α and $\gamma = 90.0000°$, $\beta = 106.9790°$, and $Z = 12.00$. Finally, the PVA/GO sample containing 6% w/w of CPX revealed the (101) and (10$\bar{1}$) characteristic peaks of PVA at the 2θ value of 20.04° and (111) diffraction of CPX at 7.96°. The latter, along with the absence of GO diffraction, confirms the successful loading of GO and CPX as well as their homogenous dispersion within the PVA polymeric matrix.

The surface morphological characteristics of the prepared films were investigated using FESEM analysis. The resultant images at two magnifications (100 μm and 200 nm) are depicted in Fig. 4. The neat PVA film showed an almost completely smooth surface with some tiny particles visible on its surface. The presence of these particles could be attributed to impurities from the starting PVA materials or the glass molds used for preparing the films. However, the addition of GO and CPX to the PVA films resulted in rough surfaces with several aggregated particles and pores that were uniformly distributed all over the sample's surface. Therefore, incorporation of GO and CPX reduced the smoothness of the PVA and resulted in a more irregular surface topology. However, as we can see in the images with higher magnification, the GO and CPX are completely fused to the PVA surface and entirely coated with PVA material. These results confirm the successful incorporation of the GO and CPX within the PVA thin films. It is worth mentioning that the PVA/GO/CPX films displayed more uniform and smoother surface structure than the PVA/GO films, which implies that the addition of CPX significantly improved the GO distribution within the PVA thin films.

The existence and relative ratio of each component in the prepared thin films were investigated by EDX analysis. From the
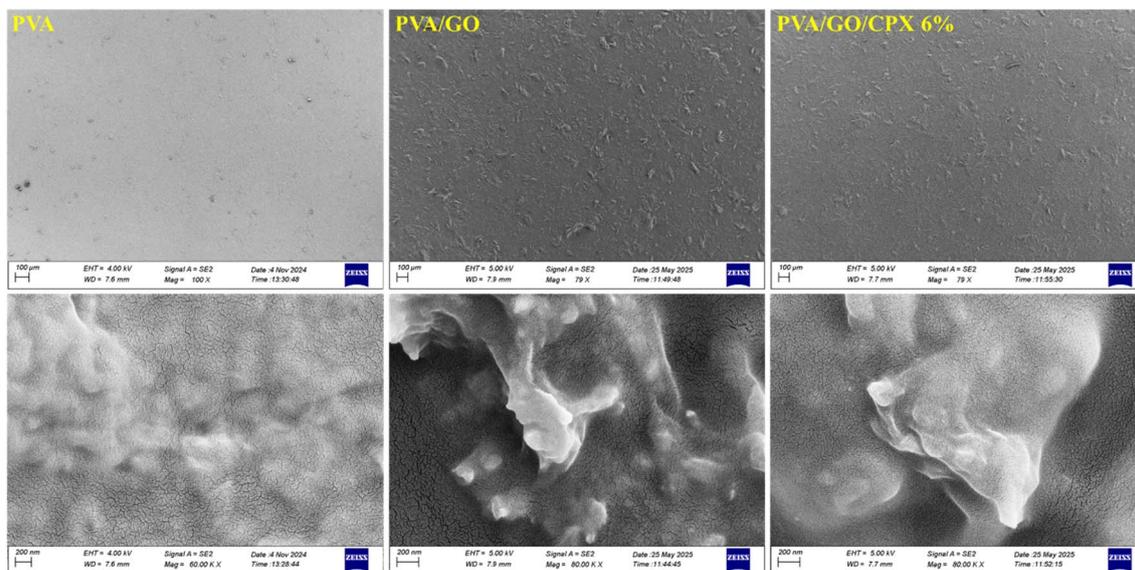
Fig. 4   FESEM images of the prepared thin films at two magnifications (top row: 100 μm and bottom row: 200 nm).

combined and individual mapping results of each element in Fig. 5, all the studied elements (C, O, N, and S) displayed a uniform distribution throughout the sample's structures. These results indicated that all starting materials were thoroughly mixed and evenly combined during the solution preparation and thin film formation processes. The uniform distribution of the thin film's components, and especially that of the loaded drug, guarantees the stable and tunable drug

release and, hence, uniform wound healing functionality. Given its hydrophilic nature, CPX is fully compatible with aqueous polymer solutions, enabling direct incorporation into PVA-based casting systems without the need for additional solvents, surfactants, or specialized solubilization steps. This property facilitates uniform drug dispersion within the prepared films. The map sum spectrum of samples and their relative weight ratios are also shown in Fig. 5. It is evident that
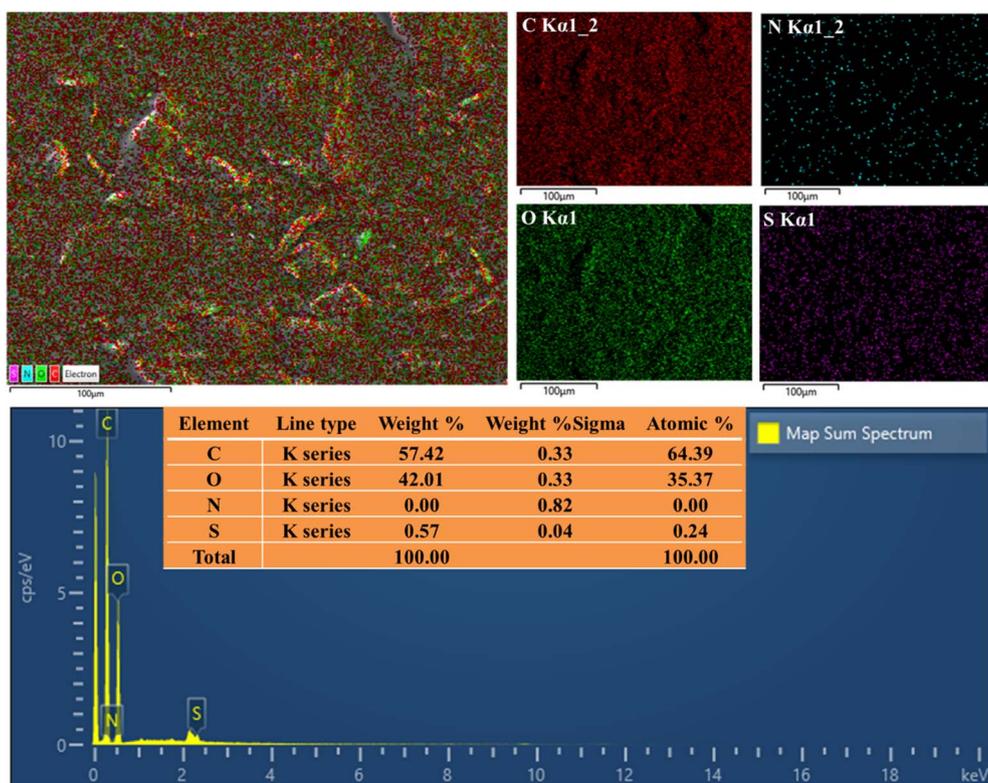

Fig. 5   EDX analyses of PVA/GO/CPX 6% thin films.

the carbon and oxygen elements exhibit higher intensities and weight ratios than nitrogen and sulfur elements. This is because of the organic and polymer-based nature of the thin film's starting materials (PVA) and also the minuscule amounts of the drug (CPX) loaded within the samples.

The thermal properties of the samples were investigated by DSC, TGA, DTA, and DTG analyses. The DSC thermograms of all the prepared thin films and pristine CPX are depicted in Fig. 6, and their major thermal transitions are summarized in Table 1. DSC analysis can be applied to study the thermal properties of the polymers and detect the presence or absence of a crystalline drug in different matrices.[69,70] The pure PVA film showed two peaks at 45.48 and 221.82 °C, corresponding to its T_g and T_m points. Moreover, three endothermic peaks were identified for the pure PVA film at 269.93 °C, 345.20 °C, and 422.77 °C, which were attributed to PVA thermal degradation (T_{Deg}). It is reported that the thermal degradation of PVA occurs in two stages, namely, dehydration and chain scission. In the first stage, which occurs at 130–260 °C, the elimination of hydroxyl groups and residual acetate groups leads to dehydration and formation of polyene structures. The second stage, at 250–385 °C, involves chain scission reactions, side reactions, cyclization reactions, and the continued degradation of the residual organic composition of PVA. Therefore, the results obtained in this study coincide well with the reported degradation profile of PVA in previous studies.[71,72] Incorporating GO within PVA thin films

increased their T_g and T_{Deg} to 88.65 °C and 338.40 °C and 421.59 °C, respectively, while decreasing the melting point to 215.70 °C. These results indicate the positive effect of GO on the thermal properties of PVA films and its homogenous dispersion throughout the sample's structure. Moreover, it is worth mentioning that, despite the T_m of the PVA/GO sample being shifted to lower temperatures compared with that of pure PVA films, the melting enthalpy of PVA/GO increased significantly from 28.54 to 84.51 J g^{-1}, implying a higher crystallinity for GO-containing samples. This confirms the enhanced and improved crystallinity of the samples following the addition of GO, as indicated in the XRD analysis section. Similar observations were also reported for PVA/GO samples, as well as the other forms of graphite-based materials, such as PVA/CNT, in previous studies.[73,74] The higher crystallinity of GO-containing samples indicates that the polymer chains were immobilized by hydrophobic and/or hydrogen bonding interactions with the graphene nanoplatelets, an effect that could support the enhanced thermal stability of the resultant composites. The DSC thermogram of pure CPX displayed an endothermic peak at 50.76 °C due to the removal of moisture and unbonded water molecules from its structure, while a second peak at 114.96 °C is related to the dehydration of its structural water molecules (monohydrate form). The T_m of CPX was observed around 229.36 °C, with a characteristic decomposition peak at 526.25 °C. Variable T_m points have been reported for CPX on scientific and commercial
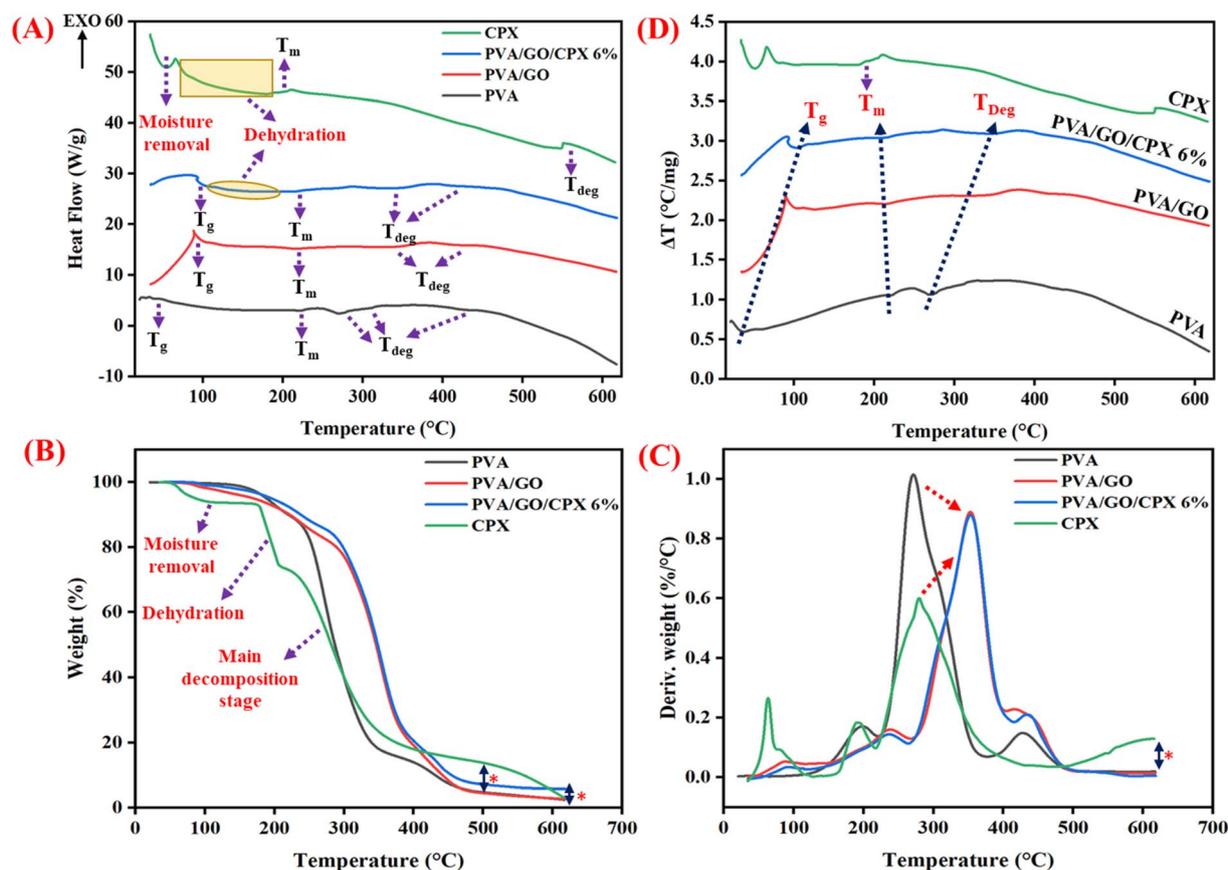

Fig. 6 Thermal properties of the samples. (A) DSC, (B) TGA, (C) DTG, and (D) DTA analyses.

Table 1 Thermal characteristics of the starting materials and fabricated thin films determined by DSC analysis

Samples	T_g/°C	T_m/°C	T_{Deg}/°C	ΔH_m/J g^{-1}	X_c/%
PVA	45.48	221.82	269.93, 345.20, 422.77	28.54	20.59
PVA/GO	88.65	215.70	338.40, 421.59	84.51	60.97
PVA/GO/CPX 6%	84.36	168.38	268.20, 342.61, 411.55	9.25	6.67
CPX	—	229.36	526.25	42.08	—

sites as well as various studies ranging from 161 to 326 °C, depending on its type (anhydrate and monohydrate) and its origin 75–77. Loading of CPX within PVA/GO films shifted all the thermal parameters of the resultant films (T_g, T_m, and T_{Deg}) to lower temperatures. Moreover, the melting enthalpy of the PVA/GO films was significantly decreased by the addition of CPX from 84.51 to 9.25 J g^{-1}, which is because of the lower melting enthalpy of pure CPX (42.08 J g^{-1}) and its powdery form that acts as an impurity within the polymeric substrate.[71,78] Finally, the T_{Deg} points of PVA/GO (338.40 and 421.59 °C) and PVA/GO/CPX films (268.20, 342.61, 411.55 °C) were observed in the DSC thermogram of each sample, which are in good agreement with the previously reported two-stage degradation of PVA materials. Finally, it is evident from Table 1 that the crystallinity of the films was increased by the addition of GO, while a reduction in the crystallinity of the samples was observed upon the addition of CPX. The reduction in crystallinity upon drug incorporation likely arises from molecular interactions between cephalexin and the PVA/GO network, which can disrupt the regular arrangement of polymer chains and hinder crystal formation. Such interactions may include hydrogen bonding between the drug's functional groups and the hydroxyl-rich PVA backbone, as well as possible surface interactions with GO.

The TGA and DTG profiles of thin films and pure CPX are illustrated in Fig. 6B and C, respectively, and their main thermal characteristics are summarized in Table 2. As we can see, all the fabricated thin films display a four-step thermal degradation behavior in the temperature range 21–650 °C. The first stage thermal degradation of samples from 21 to about 280 °C was attributed to the release of moisture and volatile compounds from the internal structure of the films, which accounts for approximately 10–20% of the weight loss of the samples. Rapid thermal degradation of samples occurs in the second step within the temperature range 230–390 °C, and a weight loss of around 60–70% was observed for all samples. This weight loss is related to the structural decomposition and degradation of the PVA films.[79,80] The third and fourth degradation stages were attributed to the further pyrogenic decomposition of the unstable residues created in the second degradation stage of the

samples. From Table 2, it is evident that all the prepared thin films resulted in approximately the same residual weight at the end of the experiment due to their organic and carbonaceous nature. The pure CPX also exhibited a four-step degradation profile from 21 to 650 °C. The first decomposition stage, at 21–175.94 °C, corresponds to the removal of moisture and chemisorbed water molecules from the CPX structure. The dehydration of the sample, with the loss of one water molecule from the composition of the hydrate, took place in the second degradation stage in the temperature range 176.00–208.24 °C, which coincides with the results obtained from DSC analysis. The third process, at 209.00–368.78 °C, involves the destruction of the cephalosporin molecule, with most parts of the CPX molecule decomposing at this stage (53.46%). In the fourth stage, the degradation of remaining composition and unstable residues from the previous stages takes place until 615.76 °C. From Fig. 6B and C and Table 2, we can see that the pure CPX and drug-containing films show slightly higher residual weights than drug-free samples (indicated by a single asterisk).[75,76] This could be related to the sulfur content of CPX, which renders a composition that is less volatile and more resistant to degradation at high temperatures. These results clearly indicate the successful loading of CPX within the prepared films.[81,82] It is worth mentioning that the addition of GO to the samples significantly increased their thermal stability (shifted to higher temperatures), as is evident from the DTG profiles of the samples (indicated by dotted red arrows).

The DTA analyses of the films (Fig. 6D) revealed similar profiles to those of the DSC thermograms (Fig. 6A). From this figure and in agreement with the results obtained from DSC analysis, it can be concluded that the T_g and T_{Deg} points of thin films were increased with the incorporation of GO and CPX within the films. On the other hand, the T_m of the films shifted to slightly lower temperatures by the addition of GO and CPX. However, the melting enthalpies of the resultant films displayed the opposite trend with their T_m points by incorporation of GO and CPX. As discussed above, the elevated T_g, T_{Deg}, and melting enthalpies of the composite films, as well as their higher residual weights from TGA analysis, confirm their improved

Table 2 Thermal properties of the samples, as obtained from the TGA and DTG analysis results

| Samples	Step 1 T (°C)	WL (%)	Step 2 T (°C)	WL (%)	Step 3 T (°C)	WL (%)	Step 4 T (°C)	WL (%)	Residual weight (%)
PVA	21.00–231.59	11.71	232.00–350.88	70.37	351.00–454.75	11.21	455.00–617.39	4.19	2.52
PVA/GO	21.00–279.77	18.40	280.00–391.94	60.61	392.00–468.87	15.14	469.00–616.27	3.14	2.71
PVA/GO/CPX 6%	21.00–280.13	15.37	281.00–391.75	62.23	392.00–465.26	13.64	466.00–617.97	2.99	5.77
CPX	21.00–175.94	7.04	176.00–208.24	18.78	209.00–368.78	53.46	369.00–615.76	17.52	3.20
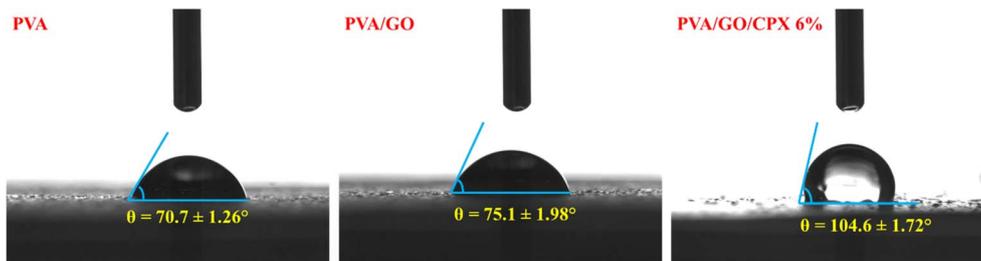
Fig. 7 Water contact angle images of the fabricated PVA, PVA/GO, and PVA/GO/CPX 6 thin films.

thermal stability compared to pure PVA thin films. An identical thermal behavior based on DSC and DTA analysis was also observed for pristine CPX, as evident from Fig. 6A and D.

The contact angle measurements provide valuable information regarding the interaction of the scaffolds with water or other liquids and reveal whether the material is hydrophilic or hydrophobic. Fig. 7 displays the contact angle of the pure PVA, PVA/GO, and PVA/GO/CPX 6%. The results showed that the pure PVA films have higher interaction with the water drop ($\theta = 70.7°$), and the contact angle of the prepared films increased by the incorporation of GO and CPX ($\theta = 75.1°$ and $104.6°$, respectively). The contact angle of PVA was reported to be in the range of 45° to 70°, indicating a hydrophilic surface. The higher contact angle of the PVA film in this study was attributed to its highly hydrolyzed nature (fully hydrolyzed PVA).[83] Moreover, increasing or decreasing the contact angle of the PVA scaffolds by the addition of GO was highlighted in previous studies, depending on the GO concentration and the specific conditions. In this regard, it is shown that the small amounts of GO can increase hydrophilicity (decrease contact angle), while higher concentrations can lead to increased roughness and potentially increased contact angles.[84,85] However, the increase in the contact angle of the films is more pronounced by the addition of CPX, and a 29.5° augmentation in contact angle value was observed for the resultant films. By considering the moderately hydrophilic nature of the CPX, these results could be explained by its better interaction with PVA than GO, which makes the hydrophobic GO more accessible and leads to an increase in the water contact angle.

The aqueous stability and swelling ratio of the films were investigated by gravimetric analysis; the results are depicted in Fig. 8A and B, respectively. It can be seen that all the prepared samples exhibit similar degradation and swelling profiles due to the common and major component (PVA) used in their preparation process. However, it is evident that the PVA/GO sample showed higher aqueous stability and, therefore, a higher swelling ratio than the other samples. This highlights the reinforcement effect of the GO in the prepared thin films, which results in higher stability. On the other hand, the CPX-containing films exhibited higher degradation and thereby lower swelling percentage in comparison to the drug-free samples. Moreover, a pH-dependent behavior was observed for all the prepared thin films. In this regard, the fabricated films exhibited higher degradation and lower swelling ratios at

lower pH values (pH 5.5). Nonetheless, all the fabricated thin films displayed a desirable swelling ratio in both pH values (greater than 1000%), which is highly beneficial in medical and biomedical applications such as wound healing.

In the next step, the release profiles of CPX from thin films were investigated in PBS media with two different pH values (5.5 and 7.4). To this end, the calibration curves of CPX in two media were established using UV-vis spectroscopy at 275 nm. From Fig. 9A and B, a good linearity with a high correlation coefficient (R^2) was obtained at the studied concentration range (10–200 ppm). The drug release profiles of CPX from the fabricated thin films in Fig. 9C and D show two distinctive release behaviors at pH 7.4 and 5.5. As we can see, a two-stage release behavior is observed at pH 7.4, while the CPX liberation at pH 5.5 occurs in a single stage. In this regard, a fast CPX release at pH 7.4 is observed in the first stage up to 120 min, followed by a slower release profile in the second stage. However, a single and fast release profile is observed at pH 5.5 throughout the entire duration of the experiment. This can be attributed to the higher degradation of the films at pH 5.5, which confirms that the liberation of CPX takes place through a matrix degradation mechanism. In general, more than 90% of CPX was released at pH 5.5 at the end of the experiment compared to 80% CPX liberation at pH 7.4. These results confirm a pH-dependent behavior for the resultant thin films, which enables controlled drug release by pH variation.

To further evaluate the drug release behavior of the obtained scaffolds, their drug release mechanisms were studied by fitting the release data to the different release kinetic equations, including zero-order, first-order, Higuchi, and Korsmeyer–Peppas models. The model parameters and correlation coefficient (R^2) values of the respective models were determined in PBS solutions at pH 7.4 and 5.5, and the results are summarized in Table 3. The first-order model did not result in the desired fitting procedure (negative fitting parameters for R^2, Q_0, and K_l) and therefore the corresponding parameters are not included in Table 3. According to the R^2 values listed in Table 3, the Higuchi model showed moderate fitting to the obtained datasets. However, the best fitting results were observed for the zero-order and Korsmeyer–Peppas models, with R^2 values greater than 0.95. It can be seen that, of these two models, the Korsmeyer–Peppas model best described the CPX release profiles of the scaffolds. Thus, the Korsmeyer–Peppas fitted release diagrams, obtained fitting equations, and R^2 values for different
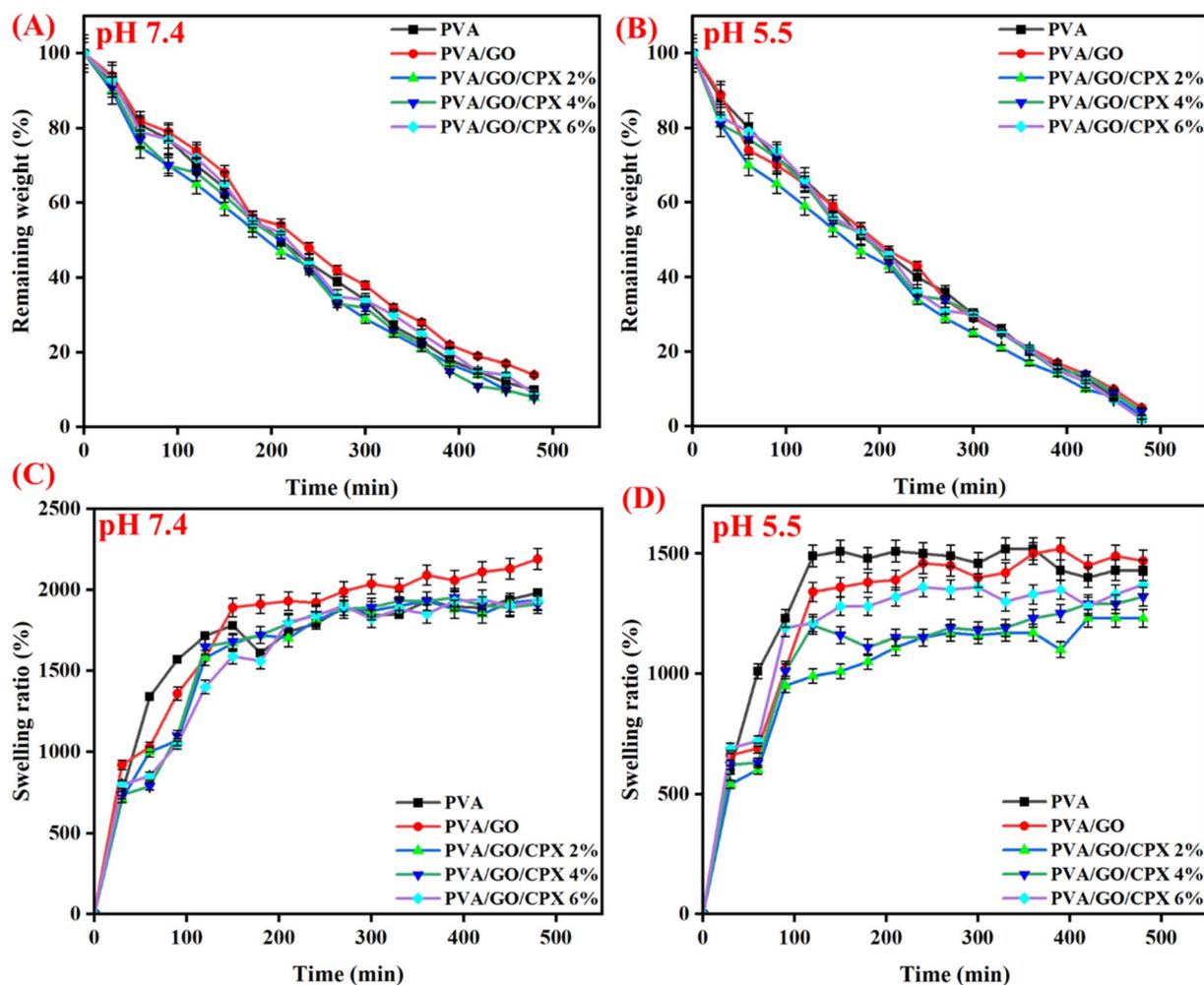
Fig. 8 (A and B) Degradation profiles and (C and D) swelling ratios of the prepared films at two different pH values.

CPX-loaded scaffolds at various concentrations are displayed in Fig. 10. As we can see, the Korsmeyer–Peppas kinetic model properly fitted the release data of all the fabricated scaffolds. Furthermore, the values of the release exponent (n) of the Korsmeyer–Peppas model (Table 3 and Fig. 10) are in the range of 0.51–0.67 for prepared thin films in both mediums, which indicates that the release followed an anomalous transport (non-Fickian diffusion) mechanism ($0.45 < n < 1$).[55] According to this mechanism, in addition to diffusion, other mechanisms may also contribute to the release of CPX from the fabricated films. By referring to Table 3, one can conclude that the R^2 values of the studied models were improved to some extent in PBS media with a lower pH (5.5). These results, along with the higher degradation of the prepared thin films in acidic media (pH 5.5), may support the hypothesis that the CPX release from the scaffolds mainly occurs through drug diffusion and erosion of the polymeric matrix.

Antibacterial activity

The antibacterial activity of the selected films (PVA, PVA/GO, and PVA/GO/CPX 6%) was evaluated using the disk diffusion test against *S. aureus* and *E. coli* bacteria. As described in the

Materials and Methods section, the fabricated films were punched into circular samples (0.5 cm in diameter) for antibacterial evaluation. However, owing to PVA's high hydrophilicity and water-absorbing properties, the films underwent noticeable shrinkage and, in some cases, detached from the culture medium surface. This resulted in significant size variation among the films, which hampers the precise interpretation of their antibacterial performance.[22,86] This limited physical stability is a significant drawback of PVA-based films in aqueous environments, underscoring the need for further material optimization in future studies. Nevertheless, as shown in Fig. 11, the PVA and PVA/GO samples exhibited no antibacterial activity against the two studied bacterial strains. On the other hand, the drug-containing films (PVA/GO/CPX 6%) exhibited a significant inhibition zone diameter against both bacteria. In this regard, the PVA/GO/CPX 6% sample resulted in 19 mm and 39 mm inhibition zone diameters against *E. coli* and *S. aureus* bacteria, respectively. Consequently, our results confirmed the suitable antibacterial activity of the fabricated films against both Gram-negative and Gram-positive bacteria. Moreover, it can be seen that higher antibacterial activity was observed against Gram-positive bacteria than Gram-negative bacteria.
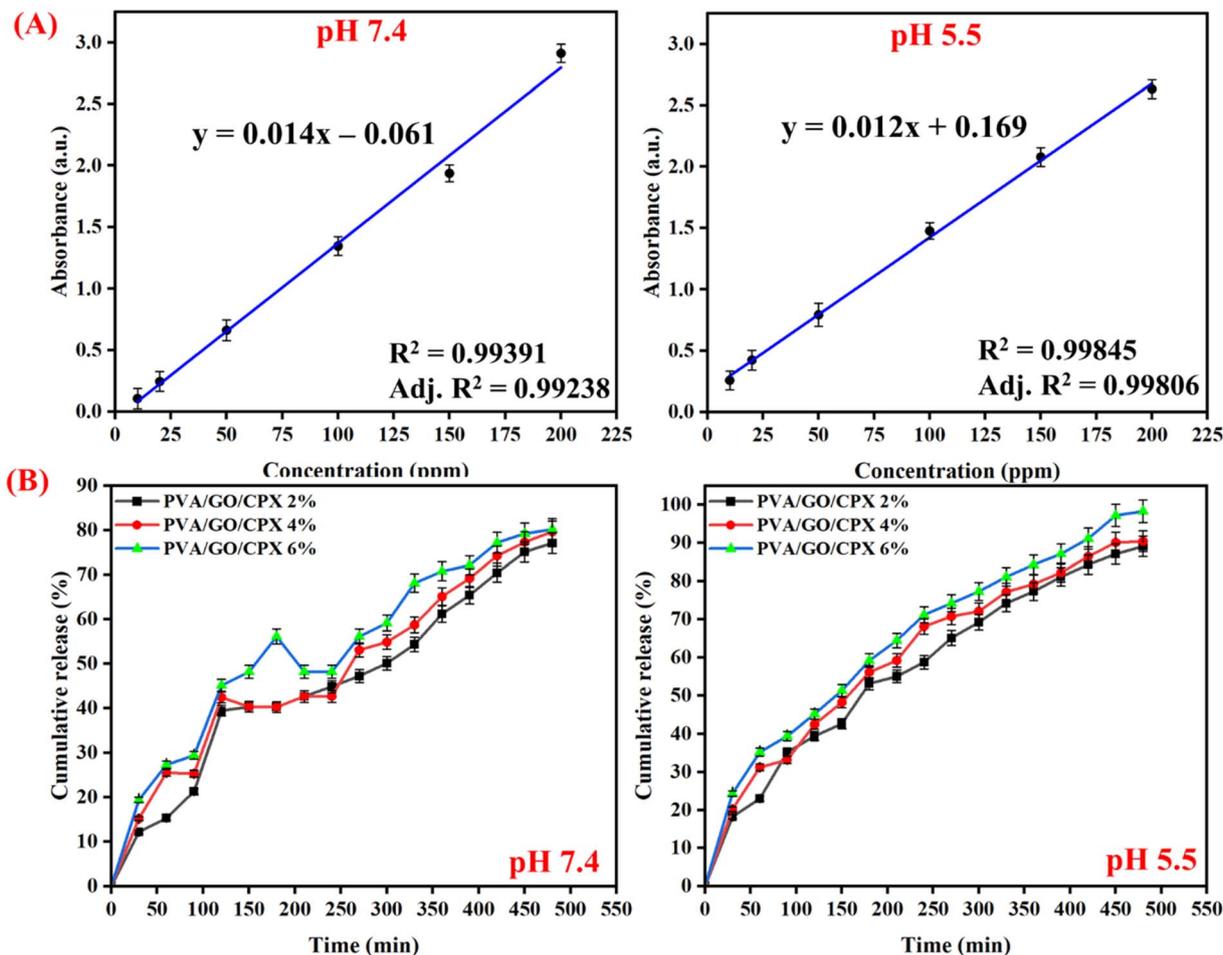
Fig. 9 (A and B) Calibration curves of CPX at pH 7.4 and 5.5. (B and C) Release profiles of CPX from the fabricated thin films containing different amounts of CPX at pH 7.4 and 5.5.

Table 3 *In vitro* release kinetic values of CPX-loaded thin films obtained using different kinetic models

Codes	Zero order			Higuchi (diffusion)		Korsmeyer–Peppas		
	R^2	Q_0	K_0	R^2	k_h	R^2	k_m	n
pH = 7.4								
PVA/GO/CPX 2%	0.935	18.71	0.17	0.892	0.35	0.971	1.23	0.67
PVA/GO/CPX 4%	0.949	12.76	0.14	0.856	0.37	0.968	1.73	0.61
PVA/GO/CPX 6%	0.909	17.76	0.14	0.732	0.39	0.969	3.35	0.51
pH = 5.5								
PVA/GO/CPX 2%	0.962	15.23	0.17	0.861	0.43	0.996	2.23	0.60
PVA/GO/CPX 4%	0.933	18.71	0.17	0.794	0.45	0.994	3.23	0.54
PVA/GO/CPX 6%	0.941	21.17	0.18	0.773	0.48	0.997	3.84	0.52

This difference in the antibacterial activity of films against the two studied bacterial strains is attributed to their differences in structure, morphology, and cell wall components. For example, Gram-positive bacteria possess a higher cell wall thickness and denser peptidoglycan layer than Gram-negative bacteria, which are mostly surrounded by tightly packed lipopolysaccharides

(LPS) and an outer membrane.[87–89] These differences in the cell structure of the different bacterial strains significantly alter their interaction with antibacterial substances and lead to differences observed in antibacterial testing for these two types of bacteria. The antibacterial activity of the fabricated films was also studied by the viable cell count method against the Gram-positive and Gram-negative bacterial strains. As shown in Fig. 12C and Table 4, all the prepared thin films demonstrated time-dependent bactericidal activity against both bacterial strains, and their bactericidal activity increased with increasing incubation time. Among the tested samples, the drug-containing film (PVA/GO/CPX 6%) exhibited superior antibacterial activity at all time points (1, 3, and 6 h). Moreover, it is evident that the fabricated thin films exhibited higher antibacterial activity against Gram-positive microorganisms (*S. aureus*) than against Gram-negative bacteria (*E. coli*). As discussed above, this difference in the antibacterial activity of the samples against the studied bacterial strains stems from the different structure, morphology, and cell wall components of Gram-positive bacteria compared to Gram-negative bacteria.[87–89] Therefore, it can be concluded that the thin film components, as well as the loaded CPX drug, strongly interfere with the
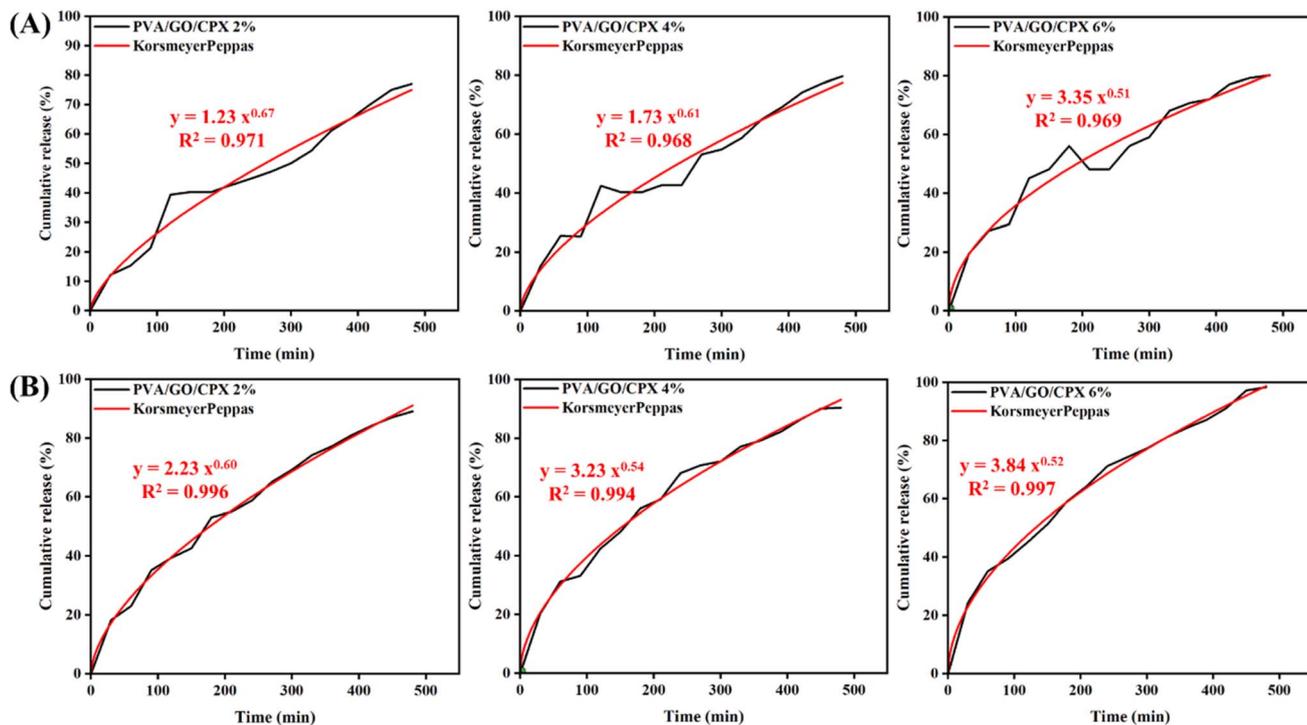
Fig. 10 Drug release data fitted to the Korsmeyer–Peppas model obtained from the drug release studies of the CPX-loaded thin films in PBS solutions at (A) pH 7.4 and (B) pH 5.5.
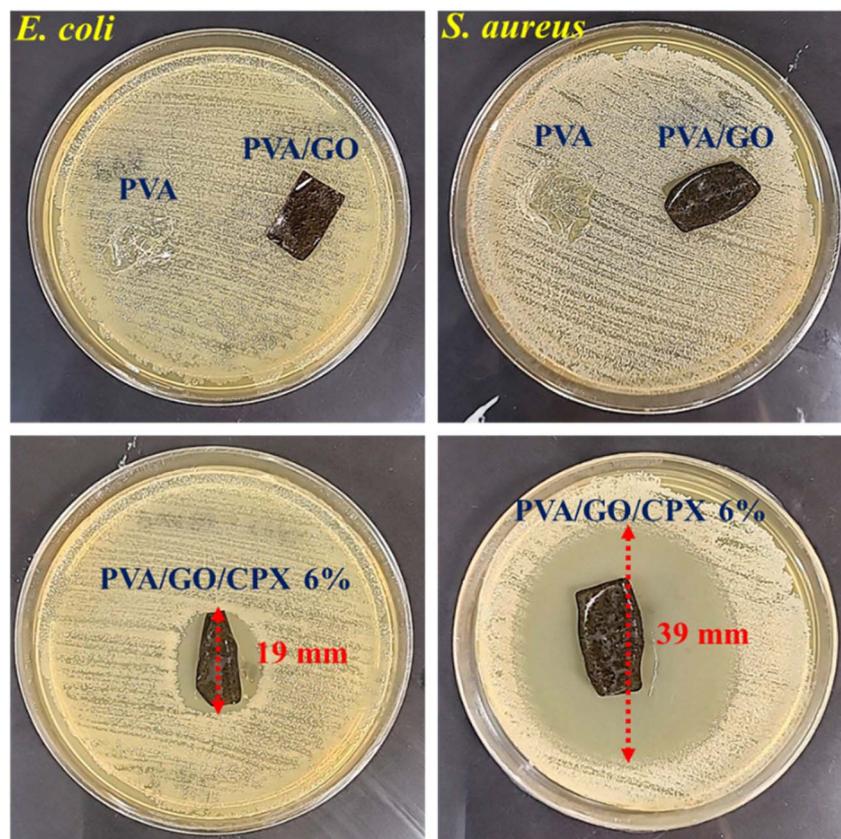

Fig. 11 Antibacterial activity of PVA, PVA/GO, and PVA/GO/CPX 6% against *S. aureus* and *E. coli* using the disk diffusion test.
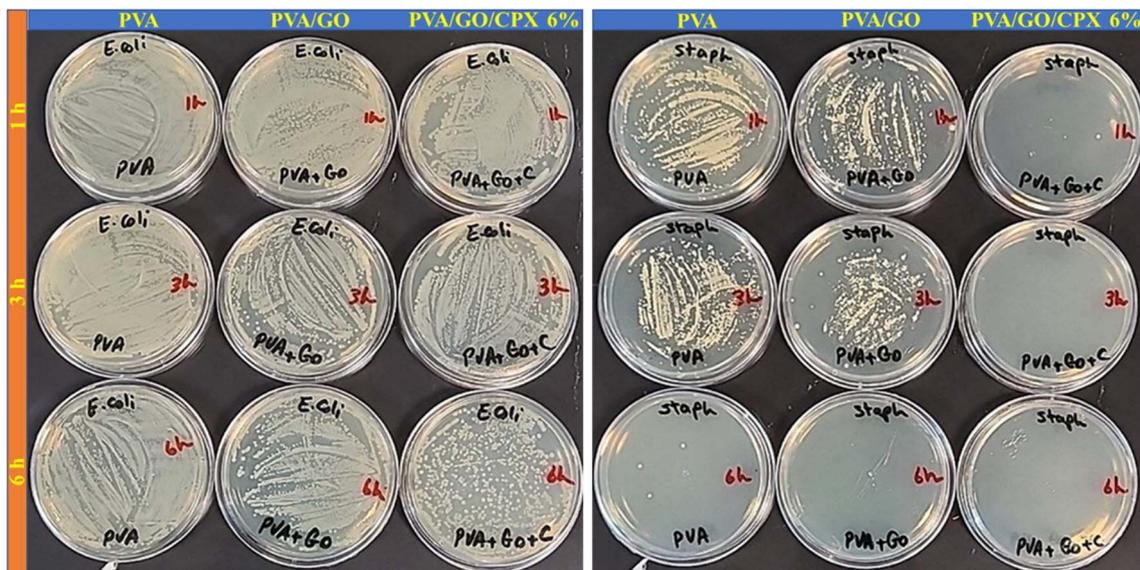
Fig. 12 Representative images of the antibacterial activity of PVA, PVA/GO, and PVA/GO/CPX 6% against *S. aureus* and *E. coli*, measured by the viable cell count method.

bacterial cell membrane permeability and normal function, eventually leading to cell death. On the other hand, it is surprisingly found that drug-free samples (PVA and PVA/GO) also exhibited good antibacterial activity, especially at more extended periods. Although no antibacterial properties have been reported for neat PVA materials, the antibacterial potency of GO has been highlighted against a variety of bacteria, including both Gram-positive and Gram-negative strains, in

previous studies.[90,91] This mild antibacterial effect of PVA and PVA/GO could arise from indirect mechanisms. PVA is highly hydrophilic and forms a gel-like surface when hydrated. This can limit bacterial adhesion and reduce microbial growth on the material surface, giving the impression of a weak antibacterial activity. On the other hand, as mentioned earlier, graphene oxide is known to exhibit moderate antibacterial behavior through physical membrane disruption caused by the

Table 4 Results of the viable cell count method for determining the antibacterial activity of PVA, PVA/GO, and PVA/GO/CPX 6% against *S. aureus* and *E. coli*[a]

Gram positive bacteria

| | Strain: *S. aureus* | | | ATCC 25923 | | | | | |
| | 1 h | | | 3 h | | | 6 h | | |
Sample	VC^1 (CFU mL^{-1})	RP^2 (%)	LR^3 (Log$_{10}$)	VC^1 (CFU mL^{-1})	RP^2 (%)	LR^3 (Log$_{10}$)	VC^1 (CFU mL^{-1})	RP^2 (%)	LR^3 (Log$_{10}$)
PVA	7×10^5	30	0.155	5×10^5	50	0.301	$<1 \times 10^2$	>99.9	>4.000
PVA/GO	4×10^5	60	0.398	3×10^5	70	0.523	$<1 \times 10^2$	>99.9	>4.000
PVA/GO/CPX 6%	$<1 \times 10^2$	>99.9	>4.000	$<1 \times 10^2$	>99.9	>4.000	$<1 \times 10^2$	>99.9	>4.000

Gram negative bacteria

| | Strain: *E. coli* | | | ATCC 25922 | | | | | |
| | 1 h | | | 3 h | | | 6 h | | |
Sample	VC^1 (CFU mL^{-1})	RP^2 (%)	LR^3 (Log$_{10}$)	VC^1 (CFU mL^{-1})	RP^2 (%)	LR^3 (Log$_{10}$)	VC^1 (CFU mL^{-1})	RP^2 (%)	LR^3 (Log$_{10}$)
PVA	$>9.5 \times 10^5$	<5	<0.022	$>9.5 \times 10^5$	<5	<0.022	9.5×10^5	5	0.022
PVA/GO	9.5×10^5	5	0.022	9×10^5	10	0.046	8×10^5	20	0.097
PVA/GO/CPX 6%	9×10^5	10	0.046	8×10^5	20	0.097	1×10^5	90	1.000

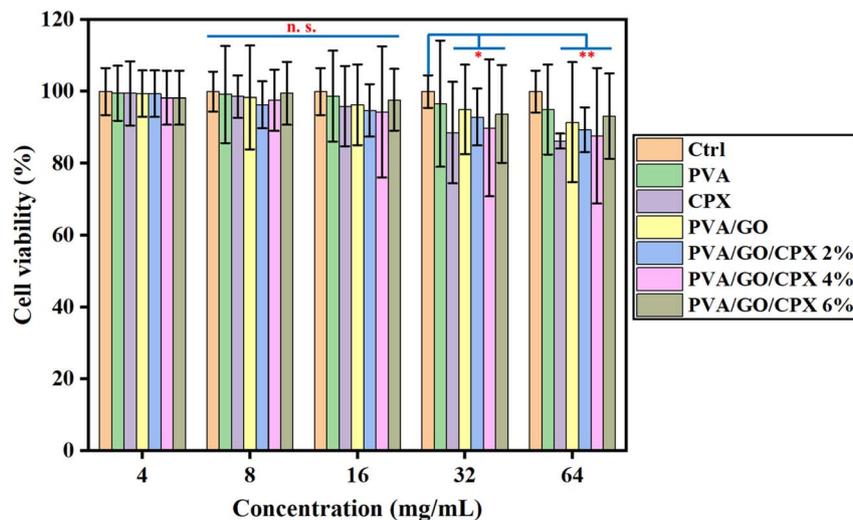[a] 1-Viable count, 2-Reduction percentage, 3-Logarithmic reduction.

Fig. 13 Cell viability of the studied samples using the MTT assay toward the HFF-1 cell line. (n. s.: not significant, *$P < 0.05$, **$P < 0.01$ vs. control).

sharp GO nanosheets, generation of reactive oxygen species (ROS), and adsorption of bacterial components, which can impair cell function. These mechanisms can suppress bacterial proliferation even in the absence of antibiotics. Therefore, the limited antibacterial activity observed in PVA and PVA/GO films is not due to strong bactericidal properties but rather to surface-related effects (PVA) and intrinsic physicochemical interactions (GO). The significant antibacterial effect reported in this study arises primarily from CPX incorporation, not from the polymer matrix itself.

The cytocompatibility of the fabricated thin films was investigated via MTT assay toward the HFF-1 normal human cell line and compared with the control group (no treatment). The cell lines were exposed to different concentrations (4, 8, 16, 32, and 64 mg mL^{-1}) of the aforementioned samples (dissolved in PBS solutions for 24 h and subsequently homogenized), and cell viability percent was monitored over 24 h. From the results presented in Fig. 13, all samples displayed the desired cytocompatibility, with more than 80% cell viability. However, upon increasing the concentration, the cell viability percentage of all samples decreased proportionally. Among the studied samples, the pure PVA film exhibited higher cell viability, and the cytocompatibility of thin films was diminished by the addition of GO and CPX. Regarding the different concentrations of CPX (2, 4, and 6% w/w), the 4% w/w CPX sample displayed the lowest cell viability compared to the 2% and 6% w/w-containing thin films. The higher cell viability percent of PVA/GO/CPX 6% could be attributed to the efficient loading and firm displacement of the drug within the thin film matrices at this concentration, along with its lower proportional drug release to the culture medium. This hypothesis could be confirmed by the similar release profiles and almost identical amounts of liberated drug that were observed in the drug release experiments. Moreover, it should be mentioned that the differences observed in the cell viability percent of the films with various concentrations of the drug were not statistically significant. On the other hand, the drug-containing thin films exhibited a higher cell viability percentage than the free drug at the same studied concentrations. Therefore, it could be concluded that the incorporation of CPX within the polymeric scaffolds enhances its
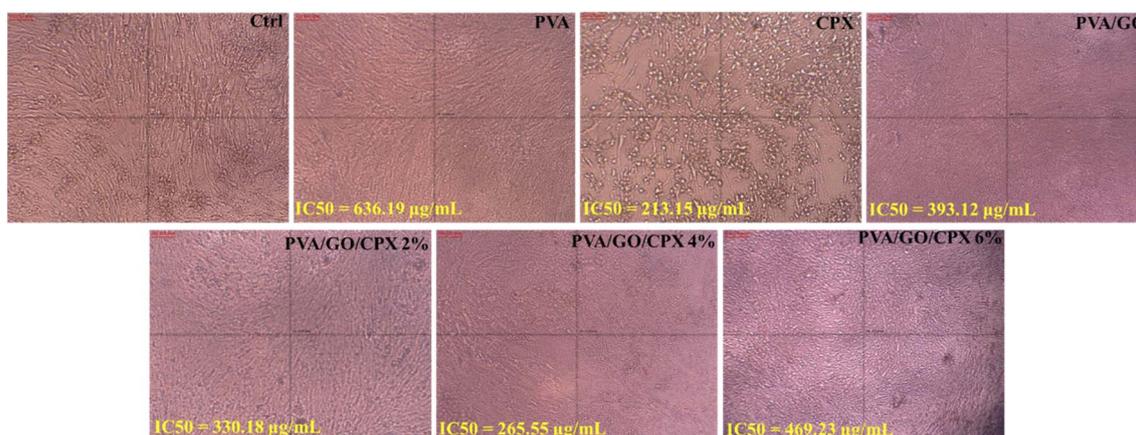

Fig. 14 Images of the HFF-1 cells treated with 64 mg mL^{-1} of the samples after 24 h and the corresponding IC50 values of the samples.

cytocompatibility toward the intended cell lines. Images of the HFF-1 cells treated with 64 mg mL^{-1} of the samples after 24 h are illustrated in Fig. 14, and the corresponding IC50 values of the samples were also provided in this figure. As we can see, all samples resulted in good cell viability and higher IC50 values at the intended concentration and time interval, indicating their desired levels of safety and cytocompatibility. It is worth mentioning that the morphology of the cells treated with the solutions of thin films is almost identical to that of the control (no treatment). On the other hand, treating the HFF-1 cells with free drug (CPX) significantly altered their morphology and shape. These results highlight the proliferative and protective characteristics of the fabricated thin films through controlling and sustaining the liberation of the drug into the culture media. In conclusion, the cytotoxicity analysis in this study revealed a high safety and cytocompatibility for the resultant thin films, which could be considered for use in medical and biomedical applications such as wound healing.

Conclusion

In this study, PVA/GO thin films containing CPX antibiotic were successfully developed as a topical drug delivery system for application in wound management. The chemical structure and crystallinity of the samples were studied by FTIR and XRD analyses, respectively. A higher thermal stability was recorded for GO-containing scaffolds *via* DSC, TGA, DTG, and DTA techniques, while the addition of CPX significantly compromised the thermal stability of the resultant films. Moreover, the porosity and surface roughness of the films were increased by the addition of the GO and CPX, and their uniform distribution throughout the sample's structure was confirmed by EDX analyses. Additionally, the incorporation of the GO and CPX resulted in a more hydrophobic surface characteristic for the obtained films. The fabricated thin films also displayed pH-dependent degradation, swelling, and release behaviors in the PBS solutions of pH 7.4 and 5.5. Furthermore, a two-stage release profile was observed for drug-containing films, and the drug-loaded scaffolds exhibited potent antibacterial activity against both Gram-positive and Gram-negative bacteria. A desired cell viability up to 64 mg mL^{-1} during 24 h was achieved in the cytocompatibility tests, and the toxic effect of the samples increased in a concentration-dependent manner. According to the results, the fabricated PVA/GO/CPX thin films could be introduced as a potential candidate for the management of topical infections and wound healing applications.

Conflicts of interest

There are no conflicts to declare.

Data availability

All data generated or analyzed during this study are included in this published article.

References

1 M. T. Manzari, Y. Shamay, H. Kiguchi, N. Rosen, M. Scaltriti and D. A. Heller, Targeted drug delivery strategies for precision medicines, *Nat. Rev. Mater.*, 2021, **6**(4), 351–370.

2 H. Alaoui Mdarhri, R. Benmessaoud, H. Yacoubi, L. Seffar, H. Guennouni Assimi, M. Hamam, *et al.*, Alternatives therapeutic approaches to conventional antibiotics: advantages, limitations and potential application in medicine, *Antibiotics*, 2022, **11**(12), 1826.

3 R. S. Kalhapure, N. Suleman, C. Mocktar, N. Seedat and T. Govender, Nanoengineered drug delivery systems for enhancing antibiotic therapy, *J. Pharm. Sci.*, 2015, **104**(3), 872–905.

4 V. Van Giau, S. S. A. An and J. Hulme, Recent advances in the treatment of pathogenic infections using antibiotics and nano-drug delivery vehicles, *Drug Des., Dev. Ther.*, 2019, 327–343.

5 G. Muteeb, M. T. Rehman, M. Shahwan and M. Aatif, Origin of antibiotics and antibiotic resistance, and their impacts on drug development: A narrative review, *Pharmaceuticals*, 2023, **16**(11), 1615.

6 S. K. Behera, S. Das, K. G. Chengappa, A. S. Xavier and S. Selvarajan, Multiple drug intolerance syndrome: an underreported distinct clinical entity, *Curr. Clin. Pharmacol.*, 2019, **14**(2), 84–90.

7 S. Barkhordari, M. Yadollahi and H. Namazi, pH sensitive nanocomposite hydrogel beads based on carboxymethyl cellulose/layered double hydroxide as drug delivery systems, *J. Polym. Res.*, 2014, **21**, 1–9.

8 M. El-Husseiny, S. Patel, R. MacFarlane and F. Haddad, Biodegradable antibiotic delivery systems, *J. Bone Jt. Surg., Br. Vol.*, 2011, **93**(2), 151–157.

9 S. K. Nandi, P. Mukherjee, S. Roy, B. Kundu, D. K. De and D. Basu, Local antibiotic delivery systems for the treatment of osteomyelitis–A review, *Mater. Sci. Eng., C*, 2009, **29**(8), 2478–2485.

10 J. Hansson, U. Körner, K. Ludwigs, E. Johnsson, C. Jönsson and K. Lundholm, Antibiotics as first-line therapy for acute appendicitis: evidence for a change in clinical practice, *World J. Surg.*, 2012, **36**(9), 2028–2036.

11 A. Torres, J. Muir, P. Corris, R. Kubin, I. Duprat-Lomon, P. Sagnier, *et al.*, Effectiveness of oral moxifloxacin in standard first-line therapy in community-acquired pneumonia, *Eur. Respir. J.*, 2003, **21**(1), 135–143.

12 N. R. Rarokar, S. D. Saoji, N. V. Deole, M. Gaikwad, A. Pandey, C. Kamaraj, *et al.*, Preparation and formula optimization of cephalexin loaded transferosomal gel by QbD to enhance the transdermal delivery: *in vitro*, *ex vivo* and *in vivo* study, *J. Drug Delivery Sci. Technol.*, 2023, **89**, 104968.

13 M. Dallo, K. Patel and A. A. Hebert, Topical antibiotic treatment in dermatology, *Antibiotics*, 2023, **12**(2), 188.

14 L.-Y. Chong, K. Head, K. E. Webster, J. Daw, P. Richmond, T. Snelling, *et al.*, Systemic antibiotics for chronic

suppurative otitis media, *Cochrane Database Syst. Rev*, 2025, **6**(6), CD013052.

15 J. Chee, K. W. Pang, J. M. Yong, R. C.-M. Ho and R. Ngo, Topical *versus* oral antibiotics, with or without corticosteroids, in the treatment of tympanostomy tube otorrhea, *Int. J. Pediatr. Otorhinolaryngol.*, 2016, **86**, 183–188.

16 A. Mombelli and L. P. Samaranayake, Topical and systemic antibiotics in the management of periodontal diseases, *Int. Dent. J.*, 2004, **54**(1), 3–14.

17 A. Date, B. Naik and M. Nagarsenker, Novel drug delivery systems: potential in improving topical delivery of antiacne agents, *Skin Pharmacol. Physiol.*, 2005, **19**(1), 2–16.

18 A. I. Mendes, R. Rebelo, I. Aroso, V. M. Correlo, A. G. Fraga, J. Pedrosa, *et al.*, Development of an antibiotics delivery system for topical treatment of the neglected tropical disease Buruli ulcer, *Int. J. Pharm.*, 2022, **623**, 121954.

19 N. Daum, C. Tscheka, A. Neumeyer and M. Schneider, Novel approaches for drug delivery systems in nanomedicine: effects of particle design and shape, *Wiley Interdiscip. Rev.:Nanomed. Nanobiotechnol.*, 2012, **4**(1), 52–65.

20 A. Patel, H. Dodiya, P. Shelate, D. Shastri and D. Dave, Design, characterization, and optimization of controlled drug delivery system containing antibiotic drug/s, *J. Drug Delivery*, 2016, **2016**(1), 9024173.

21 P. Gao, X. Nie, M. Zou, Y. Shi and G. Cheng, Recent advances in materials for extended-release antibiotic delivery system, *J. Antibiot.*, 2011, **64**(9), 625–634.

22 M. Abazari, A. Sharafi, M. Hassan, H. R. Moghimi, S. Andalib and A. Ghaffari, Electrospun silver chloride-loaded PVA nanofibers as a potential antibacterial and electroconductive scaffold for the management of wound infection and healing, *Polym. Bull.*, 2024, **81**(16), 14921–14956.

23 F. Rafiei, H. Tabesh and F. Farzad, Sustained subconjunctival drug delivery systems: Current trends and future perspectives, *Int. Ophthalmol*, 2020, **40**, 2385–2401.

24 M. Abazari and S. M. Badeleh, Antibacterial and Electroconductive Silver Chloride-Loaded PVA-Based Electrospun Nanofibers for Wound Healing Applications, *Iran. Biomed. J.*, 2024, **28**(7), 5.

25 T. Garg, O. Singh, S. Arora and R. Murthy, Scaffold: a novel carrier for cell and drug delivery, *Crit. Rev. Ther. Drug Carr. Syst*, 2012, **29**(1), 1–63.

26 P. Ghasemiyeh and S. Mohammadi-Samani, Hydrogels as drug delivery systems; pros and cons, *Crit. Rev. Ther. Drug Carr. Syst*, 2019, **5**(1), 7–24.

27 A. K. Umar, M. Butarbutar, S. Sriwidodo and N. Wathoni, Film-forming sprays for topical drug delivery, *Drug Des., Dev. Ther.*, 2020, 2909–2925.

28 D. Chen, M. Wu, J. Chen, C. Zhang, T. Pan, B. Zhang, *et al.*, Robust, flexible, and bioadhesive free-standing films for the co-delivery of antibiotics and growth factors, *Langmuir*, 2014, **30**(46), 13898–13906.

29 S. D. Barnhart, Thin film oral dosage forms, *Modified-release Drug Delivery Technology*, CRC Press, 2008, pp. 235–56.

30 K. Kathe and H. Kathpalia, Film forming systems for topical and transdermal drug delivery, *Asian J. Pharm. Sci.*, 2017, **12**(6), 487–497.

31 V. K. Vendra, L. Wu and S. Krishnan, Polymer thin films for biomedical applications, *Nanotechnologies for the Life Sciences*, Wiley-VCH Verlag GmbH & Co. KGaA, 1st edn, 2010, vol. 5, DOI: 10.1002/9783527610419.ntls0179.

32 Y. Jang, S. Park and K. Char, Functionalization of polymer multilayer thin films for novel biomedical applications, *Korean J. Chem. Eng.*, 2011, **28**, 1149–1160.

33 S. Pawde and K. Deshmukh, Characterization of polyvinyl alcohol/gelatin blend hydrogel films for biomedical applications, *J. Appl. Polym. Sci.*, 2008, **109**(5), 3431–3437.

34 R. Kumar, K. Dinesh, S. Sunnitha and K. Punithavathi, Preparation and characterization of polyvinyl alcohol thin films for organic thin film transistors and biomedical applications, *KRJ*, 2018, **5**(2), 16–18.

35 Thai P. T. N., Pham X. M., Nguyen T. B., Le T. M., Tran C. B. V. and Phong M. T., *et al.*, Preparation and characterization of PVA thin-film composite membrane for pervaporation dehydration of ethanol solution, *IOP Conference Series: Earth and Environmental Science*, IOP Publishing, 2021.

36 B. Bolto, M. Hoang and Z. Xie, A review of membrane selection for the dehydration of aqueous ethanol by pervaporation, *Chem. Eng. Process.: Process In*, 2011, **50**(3), 227–235.

37 T. LdA. Montanheiro, V. M. Schatkoski, B. R. C. de Menezes, R. M. Pereira and R. G. Ribas, Recent progress on polymer scaffolds production: Methods, main results, advantages and disadvantages, *eXPRESS Polym. Lett.*, 2022, **16**(2), 197–219.

38 N. Jain, V. K. Singh and S. Chauhan, A review on mechanical and water absorption properties of polyvinyl alcohol based composites/films, *J. Mech. Behav. Mater.*, 2017, **26**(5–6), 213–222.

39 B. K. Tan, Y. C. Ching, S. C. Poh, L. C. Abdullah and S. N. Gan, A review of natural fiber reinforced poly (vinyl alcohol) based composites: Application and opportunity, *Polymers*, 2015, **7**(11), 2205–2222.

40 A. Verma, N. Jain, K. Singh, V. K. Singh, S. M. Rangappa and S. Siengchin, PVA-based blends and composites, *Biodegradable Polymers, Blends and Composites*, Elsevier, 2022, pp. 309–26.

41 S. Kashyap, S. K. Pratihar and S. K. Behera, Strong and ductile graphene oxide reinforced PVA nanocomposites, *J. Alloys Compd.*, 2016, **684**, 254–260.

42 K. A. Hurayra-Lizu, M. W. Bari, F. Gulshan and M. R. Islam, GO based PVA nanocomposites: tailoring of optical and structural properties of PVA with low percentage of GO nanofillers, *Heliyon*, 2021, **7**(5), e06983.

43 N. Bellier, P. Baipaywad, N. Ryu, J. Y. Lee and H. Park, Recent biomedical advancements in graphene oxide-and reduced graphene oxide-based nanocomposite nanocarriers, *Biomater. Res.*, 2022, **26**(1), 65.

44 X. Fu, J. Lin, Z. Liang, R. Yao, W. Wu, Z. Fang, *et al.*, Graphene oxide as a promising nanofiller for polymer composite, *Surf. Interfaces*, 2023, **37**, 102747.

45 N. Mushahary, A. Sarkar, F. Basumatary, S. Brahma, B. Das and S. Basumatary, Recent developments on graphene oxide and its composite materials: From fundamentals to applications in biodiesel synthesis, adsorption, photocatalysis, supercapacitors, sensors and antimicrobial activity, *Results Surf. Interfaces*, 2024, 100225.

46 A. M. Oliveira, M. Machado, G. A. Silva, D. B. Bitoque, J. Tavares Ferreira, L. A. Pinto, *et al.*, Graphene oxide thin films with drug delivery function, *Nanomaterials*, 2022, **12**(7), 1149.

47 S. R. Laraba, W. Luo, A. Rezzoug, Q. Zahra, S. Zhang, B. Wu, *et al.*, Graphene-based composites for biomedical applications, *Green Chem. Lett. Rev.*, 2022, **15**(3), 724–748.

48 Y. Xu, W. Hong, H. Bai, C. Li and G. Shi, Strong and ductile poly (vinyl alcohol)/graphene oxide composite films with a layered structure, *Carbon*, 2009, **47**(15), 3538–3543.

49 I. Taraghi, S. Paszkiewicz, I. Irska, A. Szymczyk, A. Linares, T. A. Ezquerra, *et al.*, Thin polymer films based on poly (vinyl alcohol) containing graphene oxide and reduced graphene oxide with functional properties, *Polym. Eng. Sci.*, 2021, **61**(6), 1685–1694.

50 Z. Wu, Y. Huang, L. Xiao, D. Lin, Y. Yang, H. Wang, *et al.*, Physical properties and structural characterization of starch/polyvinyl alcohol/graphene oxide composite films, *Int. J. Biol. Macromol.*, 2019, **123**, 569–575.

51 Jr W. S. Hummers and R. E. Offeman, Preparation of graphitic oxide, *J. Am. Chem. Soc.*, 1958, **80**(6), 1339.

52 M. Abazari, R. Jamjah and H. Abdollahi, Investigation of optimal condition of ethylene polymerization using a new three-metallic high-performance Ziegler–Natta catalyst: experimental design and polymer characterization, *Catal. Lett.*, 2023, **153**(2), 622–633.

53 Q. Gao, J. Luo, X. Wang, C. Gao and M. Ge, Novel hollow α-Fe 2 O 3 nanofibers *via* electrospinning for dye adsorption, *Nanoscale Res. Lett.*, 2015, **10**, 1–8.

54 M. Jafari and B. Kaffashi, Mathematical kinetic modeling on isoniazid release from Dex-HEMA-PNIPAAm nanogels, *Nanomed. Res. J.*, 2016, **1**(2), 90–96.

55 L. Ahmed, R. Atif, T. S. Eldeen, I. Yahya, A. Omara and M. Eltayeb, Study the using of nanoparticles as drug delivery system based on mathematical models for controlled release, *IJLTEMAS*, 2019, **8**(5), 52–56.

56 T. M. de Souza Pinto, F. L. A. Almeida, J. O. de Lucas Xavier, G. Del-Vechio-Vieira, A. L. S. de Matos Araújo, M. S. Alves, *et al.*, Biopharmacotechnical and physical properties of solid pharmaceutical forms containing rutin commercially acquired in Juiz de Fora city, Brazil, *Acta Sci.*, 2020, **42**, e52212e.

57 Jr R. J. Wallace, J. Dalovisio and G. Pankey, Disk diffusion testing of susceptibility of Mycobacterium fortuitum and Mycobacterium chelonei to antibacterial agents, *Antimicrob. Agents Chemother.*, 1979, **16**(5), 611–614.

58 K. Thangavel, T. Roshini, V. Balaprakash, P. Gowrisankar, S. Sudha and M. Mohan, Structural, morphological and antibacterial properties of ZnO nanofibers fabricated by electrospinning technique, *Mater. Today: Proc.*, 2020, **33**, 2160–2166.

59 N. Babayevska, Ł. Przysiecka, G. Nowaczyk, M. Jarek, M. Järvekülg, T. Kangur, *et al.*, Fabrication of gelatin-zno nanofibers for antibacterial applications, *Materials*, 2020, **14**(1), 103.

60 I. Perelshtein, G. Applerot, N. Perkas, G. Guibert, S. Mikhailov and A. Gedanken, Sonochemical coating of silver nanoparticles on textile fabrics (nylon, polyester and cotton) and their antibacterial activity, *Nanotechnology*, 2008, **19**(24), 245705.

61 M. Abazari, S. M. Badeleh, F. Khaleghi, M. Saeedi and F. Haghi, Fabrication of silver nanoparticles-deposited fabrics as a potential candidate for the development of reusable facemasks and evaluation of their performance, *Sci. Rep.*, 2023, **13**(1), 1593.

62 S. Barkhordari and A. Alizadeh, Zinc/aluminum-layered double hydroxide-gallic acid doped carboxymethyl cellulose nanocomposite films for wound healing, *Int. J. Biol. Macromol.*, 2024, **260**, 129556.

63 S. Jin, J. Li, J. Wang, J. Jiang, Y. Zuo, Y. Li, *et al.*, Electrospun silver ion-loaded calcium phosphate/chitosan antibacterial composite fibrous membranes for guided bone regeneration, *Int. J. Nanomed.*, 2018, 4591–4605.

64 T. F. Emiru and D. W. Ayele, Controlled synthesis, characterization and reduction of graphene oxide: A convenient method for large scale production, *Egypt. J. Basic Appl. Sci*, 2017, **4**(1), 74–79.

65 A. Rawal, S. H. Che Man, V. Agarwal, Y. Yao, S. C. Thickett and P. B. Zetterlund, Structural complexity of graphene oxide: the kirigami model, *ACS Appl. Mater. Interfaces*, 2021, **13**(15), 18255–18263.

66 N. Kumar, S. Das, C. Bernhard and G. D. Varma, Effect of graphene oxide doping on superconducting properties of bulk MgB2, *Supercond. Sci. Technol.*, 2013, **26**(9), 095008.

67 M. Aslam, M. A. Kalyar and Z. A. Raza, Graphene oxides nanosheets mediation of poly (vinyl alcohol) films in tuning their structural and opto-mechanical attributes, *J. Mater. Sci.: Mater. Electron.*, 2017, **28**, 13401–13413.

68 X. Yuan, Enhanced interfacial interaction for effective reinforcement of poly (vinyl alcohol) nanocomposites at low loading of graphene, *Polym. Bull.*, 2011, **67**(9), 1785–1797.

69 D. Giron. Thermal analysis of drugs and drug products. *Encyclopedia of pharmaceutical technology*. 2002;15, pp. 12–17.

70 D. Giron, Applications of thermal analysis and coupled techniques in pharmaceutical industry, *J. Therm. Anal. Calorim.*, 2002, **68**(2), 335–357.

71 B. Holland and J. Hay, The thermal degradation of poly (vinyl alcohol), *Polymer*, 2001, **42**(16), 6775–6783.

72 P. Thomas, J.-P. Guerbois, G. Russell and B. Briscoe, FTIR study of the thermal degradation of poly (vinyl alcohol), *J. Therm. Anal. Calorim.*, 2001, **64**(2), 501–508.

73 I. Tantis, G. Psarras and D. Tasis, Functionalized graphene-poly (vinyl alcohol) nanocomposites: Physical and dielectric properties, *eXPRESS Polym. Lett.*, 2012, **6**(4), 283–292.

74 K. P. Ryan, M. Cadek, V. Nicolosi, D. Blond, M. Ruether, G. Armstrong, *et al.*, Carbon nanotubes for reinforcement of plastics? A case study with poly (vinyl alcohol), *Compos. Sci. Technol.*, 2007, **67**(7–8), 1640–1649.

75 M. C. Chuong, R. Varanasi, D. Seniuk, N. Aggarwal, C. Bongiorno, S. Fdal, *et al.*, Investigation on the endothermic event of cephalexin monohydrate in differential scanning calorimetric curve, *J. Therm. Anal. Calorim.*, 2016, **123**, 2165–2172.

76 A. Fuliaș, T. Vlase, G. Vlase and N. Doca, Thermal behaviour of cephalexin in different mixtures, *J. Therm. Anal. Calorim.*, 2010, **99**(3), 987–992.

77 M. Chuong, N. Aggarwal, C. Bongiorno, S. Fdal, J. Geangu and B. MacDonald, *et al.*, Thermal Analysis of Cephalexin Monohydrate.

78 R. Wulandari, Y. A. Swasono, M. Z. N. Ichsan and A. Rifathin, Thermal Behavior and Kinetic of Degradation of PVA and PVA/CS/AL Blend, *Sainteknol*, 2023, **21**(1), 1–10.

79 V. Jadhav, C. Chakraborty and D. Nerkar, Nanoparticle-embedded polymer reparation and characterization of PVA-PPy-Au nanocomposite free standing Films, *Int J Sci Res Rev*, 2018, **7**, 136–147.

80 Ozturk M. K., Nergis B. and Candan C., *Thermal Analysis of PVA Nanofibrous Membranes. IOP Conference Series: Materials Science and Engineering*, IOP Publishing, 2018.

81 C. Thompson, R. Meyer and J. Ball, Thermal decomposition of sulfur compounds. II. 1-Pentanethiol, *J. Am. Chem. Soc.*, 1952, **74**(13), 3287–3289.

82 A. Akshatha, J. S. Rajan and H. Ramachandra, Study of degradation of sulphur compounds and depletion of metal passivators during thermal ageing of mineral oil, *IEEE Trans. Dielectr. Electr. Insul.*, 2015, **22**(5), 2786–2797.

83 B. Zuo, Y. Hu, X. Lu, S. Zhang, H. Fan and X. Wang, Surface properties of poly (vinyl alcohol) films dominated by spontaneous adsorption of ethanol and governed by hydrogen bonding, *J. Phys. Chem. C*, 2013, **117**(7), 3396–3406.

84 G. Zhang, Q. Sun, G. Zhang, L. Wang, X. Cui and M. Lv, PVA-GO-Lip hydrogel loaded alendronate sodium: friction adaptation, controlled release, antibacterial and mineralization mechanism, *J. Biomater. Sci., Polym. Ed.*, 2025, 1–22.

85 T. Lin, Y. Wu, H. Chen, X. Ren and R. Joshi, Graphene oxide-polyvinyl alcohol nanofiltration membranes for efficient dye removal in practical conditions, *J. Membr. Sci.*, 2025, **719**, 123736.

86 M. Abazari, S. M. Badeleh, S. Barkhordari, S. S. Mohammed, M. M. Ahmed, M. S. M. Ameen, *et al.*, Preparation and characterization of polyvinyl alcohol thin films: Rheological, physicochemical and functional properties, *Heliyon*, 2025, **11**(12), e43604.

87 T. J. Silhavy, D. Kahne and S. Walker, The bacterial cell envelope, *Cold Spring Harbor Perspect. Biol.*, 2010, **2**(5), a000414.

88 M. Salton, Studies of the bacterial cell wall: IV. The composition of the cell walls of some gram-positive and gram-negative bacteria, *Biochim. Biophys. Acta*, 1953, **10**, 512–523.

89 W. Jiang, A. Saxena, B. Song, B. B. Ward, T. J. Beveridge and S. C. Myneni, Elucidation of functional groups on gram-positive and gram-negative bacterial surfaces using infrared spectroscopy, *Langmuir*, 2004, **20**(26), 11433–11442.

90 S. Liu, T. H. Zeng, M. Hofmann, E. Burcombe, J. Wei, R. Jiang, *et al.*, Antibacterial activity of graphite, graphite oxide, graphene oxide, and reduced graphene oxide: membrane and oxidative stress, *ACS Nano*, 2011, **5**(9), 6971–6980.

91 J. A. Sanchez, L. Materon, J. G. Parsons and M. Alcoutlabi, Synthesis, Characterization, and Antibacterial Activity of Graphene Oxide/Zinc Hydroxide Nanocomposites, *Appl. Sci.*, 2024, **14**(14), 2076–3417.